Strong Intraseasonal Variability of Meridional Currents near 5°N in the Eastern Indian Ocean: Characteristics and Causes

Gengxin Chen[1,2], Weiqing Han[2], Yuanlong Li[2], Michael J. McPhaden[3], Ju Chen[1], Weiqiang Wang[1], Dongxiao Wang[1]

[1]State Key Laboratory of Tropical Oceanography, South China Sea Institute of Oceanology, Chinese Academy of Sciences, Guangzhou, China

[2]Department of Atmospheric and Oceanic Sciences, University of Colorado, Boulder, Boulder, Colorado

[3]Pacific Marine Environmental Laboratory, National Oceanic and Atmospheric Administration, Seattle, Washington

Corresponding Author:

Dongxiao Wang

State Key Laboratory of Tropical Oceanography, South China Sea Institute of Oceanology, Chinese Academy of Sciences, Guangzhou, China

Email: dxwang@scsio.ac.cn

Abstract

This paper reports on strong intraseasonal upper-ocean meridional currents observed in the Indian Ocean between the Bay of Bengal (BOB) and the equator, and elucidates the underlying physical processes responsible for them. In-situ measurements from a subsurface mooring at 5ºN, 90.5ºE reveal strong intraseasonal variability of meridional current with an amplitude of ~0.4 m s^{-1} and a typical period of 30-50 days in the upper 150 m, which by far exceeds the magnitudes of the mean flow and seasonal cycle. Such prominent intraseasonal variability is however not seen in zonal current at the same location. Further analysis suggests that the observed intraseasonal flows are closely associated with westward propagating eddy-like sea surface height anomalies (SSHAs) along 5ºN. The eddy-like SSHAs are largely manifestations of symmetric Rossby waves, which result primarily from intraseasonal wind stress forcing in the equatorial waveguide and reflection of the equatorial Kelvin waves at the eastern boundary. Since the wave signals are generally symmetric about the equator, similar variability is also seen at 5ºS but with weaker intensity, due to the inclined coastline at the eastern boundary. The Rossby waves propagate westward, causing pronounced intraseasonal SSHA and meridional current in the upper ocean across the entire southern BOB between 84°-94°E, They greatly weaken in the western Indian basin, but zonal currents near the equator remain ~~appreciable magnitude~~.

1. Introduction

Sea surface winds over the tropical Indian Ocean exhibit strong intraseasonal variability (ISV), which is associated with atmospheric intraseasonal oscillations (ISOs), with the Madden-Julian Oscillation (MJO) as the dominated mode (e.g., Madden and Julian 1971; Hendon and Glick 1997; Webster et al. 2002; Shinoda et al. 2013). In response to the surface wind forcing, the upper-ocean circulation of the tropical Indian Ocean shows strong intraseasonal variations (e.g., Masumoto et al. 2005). Based on in-situ observations and numerical models, several studies have reported prominent ISV of the meridional currents in the equatorial Indian Ocean (McPhaden 1982; Reppin et al. 1999; Sengupta et al. 2001; Masumoto et al. 2005; Ogata et al. 2008; Iskandar and McPhaden 2011), which contributes to seasonal-to-interannual cross-equatorial heat and salt transports (e.g., Halkides et al. 2007). Further north, there are two large marginal seas in the North Indian Ocean, namely the Arabian Sea and Bay of Bengal (BOB), with distinct water mass properties (e.g., Mamayev 1975; You and Tomczak 1993; Vinayachandran and Kurian 2007; Vinayachandran et al. 2013). The meridional ocean currents between the equatorial Indian Ocean and the two marginal seas are essential for heat, freshwater, and nutrient distributions over the tropical Indian Ocean and thereby affect the large-scale air-sea interaction (e.g., Izumo et al. 2010). However, due to shortage of direct observations, our knowledge of the meridional ocean current variability in this region is quite limited, especially at intraseasonal timescale.

A subsurface mooring system was deployed at 5ºN, 90.5ºE by the South China Sea Institute of Oceanology (SCSIO), Chinese Academy of Sciences, to monitor the upper-ocean water exchanges between the BOB and the equatorial Indian Ocean (red star in Fig. 1). During the observation period of April 2013-April 2014, a striking phenomenon is captured by the current measurements of the mooring. Strong intraseasonal variability of meridional current is detected in the Acoustic Doppler Current Profiler (ADCP) records (Fig. 2b), which is however not evident in zonal current (Fig. 2a). The meridional current anomalies have a typical amplitude of ~0.4 m s^{-1}, by far exceeding the mean flow and comparable to the major western boundary currents of the tropical Indian Ocean (e.g., Lutjeharms et al. 1981; Schott and Quadfasel 1982; Shetye et al. 1993).

The ISV of the equatorial winds over the Indian Ocean has been shown to significantly affect the adjacent areas. Intraseasonal equatorial Kelvin waves driven by winds associated with the MJO can propagate to the eastern Indian Ocean (EIO) boundary and the Indonesian Seas, affecting the ISV of sea level along Sumatra and Java coasts (Iskandar et al., 2005) and the Indonesian Throughflow (Qiu et al., 1999; Schiller et al., 2010; Pujiana et al., 2013). Subsequently, the coastal Kelvin waves are reflected back into the ocean interior as Rossby waves, which significantly influence the thermocline and sea level variations in the BOB (Cheng et al. 2013; Girishkumar et al. 2013) and the southeast Indian Ocean (Chen et al., 2015a). Upon impinging on the eastern boundary, the intraseasonal equatorial Kelvin waves, which are symmetric about the equator, are reflected back as symmetric Rossby waves in an idealized rectangular-domain model (Matsuno 1966; Moore and Philander 1977; Han et al., 2011). Due to the effects of strong shear of the zonal flow and slanted coastlines in the equatorial oceans, the meridional structures of the equatorial waves can become asymmetric (e.g., Chelton et al., 2003; Durland et al., 2010; Han et al., 2011), and thus induce asymmetric current variability on the north and south sides of the equator. Consequently, the observed ISV~~s~~ by the mooring at 90ºE, 5ºN may be affected by equatorial winds through symmetric/asymmetric Rossby waves. Careful and comprehensive analysis is required to achieve an in-depth understanding of the observed variability.

The goal of this research is to characterize and explain the observed strong ISV of meridional current near 5ºN. Satellite and in situ observations are analyzed to document the characteristics of intraseasonal currents, and ocean general circulation model (OGCM) experiments are performed to provide insight into the underlying mechanisms. The rest of the paper is organized as follows. Section 2 describes observational data utilized in this study and OGCM experiments performed for our analysis. Section 3 presents the results of our analysis, with Section 3.1 describing the observed characteristics of intraseasonal meridional currents, Section 3.2 exploring local and remote forcing effects of ISO winds, and Section 3.3 discussing essence and components of the observed current anomalies. Section 4 provides a summary and discussion for this research.

2. Data and Methods

2.1. Data

The mooring was deployed in the southern BOB at approximately 5ºN, 90.5ºE (star in Figure 1) from April 2013 to April 2014, equipped with an upward-looking 75 kHz and a downward-looking 150 kHz Workhorse Acoustic Doppler Current Profiler (ADCP) in the main float. Vertical resolution of the ADCP measurements is 8 m. Sampling time frequency of the ADCP is 1 hour. The effective measurement range covers 20-145 m and 180-570 m. In this study, the ADCP current velocities are linearly interpolated onto uniform 5 m intervals, and hourly measurements are averaged into daily data.

The Ocean Surface Current Analysis-Real time (OSCAR) product is available since December 1992 with a horizontal resolution of 1/3°×1/3° and 5-day intervals (Bonjean and Lagerloef 2002; Johnson et al. 2007) and represents the total ocean current (both geostrophic and Ekman components) of the upper 30 m. In this study, the OSCAR surface current estimate from 2001 through 2014 are used as observed surface current data. The daily 0.25°×0.25° sea surface height (SSH) and surface geostrophic current products distributed by the Archiving, Validation, and Interpretation of Satellite Oceanographic (AVISO) (Le Traon et al. 1998; Ducet et al.

2000) for 2011-2014 are analyzed to understand ISV of SSH and meridional current. The daily 0.25°×0.25° gridded Advanced Scatterometer (ASCAT) satellite ocean surface wind vectors (Bentamy and Croize-Fillon 2012) during 2011-2014 are used to understand the relationship between intraseasonal SSH anomalies (SSHA) and wind forcing of ISOs. The monthly subsurface ocean state estimate, with a horizontal resolution of 1°×1° and 42 vertical levels, of the European Centre for Medium range Weather Forecasting (ECMWF) Ocean Reanalysis System version 4 (ORAS4; Balmaseda et al. 2013) ~~data~~ available since 1958 ~~are~~ used to compute the mean thermocline depth (represented by the depth of 20°C isotherm) and calculate the first and second baroclinic modes speeds. Current measurements from two equatorial moorings of the Research Moored Array for African–Asian–Australian Monsoon Analysis and Prediction (RAMA; see McPhaden et al. 2009) are used to verify the model performance on ISV of equatorial currents. One mooring is deployed at 0, 90°E and provides data from 14 November 2000 to 7 June 2012 at depths range from 40 to 410m. The other is deployed at 0, 80.5°E and provides data from 27 October 2004 to 17 August 2012 at depths from 25 to 350m. Data are often missing at deeper layers.

2.2. OGCM and experiments

The OGCM used in this study is the HYbrid Coordinate Ocean Model (HYCOM; e.g., Wallcraft et al., 2009) version 2.2.18, which is configured to the Indian Ocean basin (30°E-122.5°E, 50°S-30°N) with a horizontal resolution of 0.25°×0.25° and 26 vertical layers (Li et al., 2014, 2015). The surface atmospheric forcing fields include 10-m winds from the cross-calibrated multi-platform (CCMP) version 1.1 product (Atlas et al. 2008), the 0.25°×0.25° ASCAT satellite ocean surface vector winds, 1°×1° surface net shortwave radiation (SWR) and longwave radiation (LWR) from the Clouds and the Earth's Radiant Energy System (CERES; Wielicki et al. 1996), 0.25°×0.25° precipitation from the Tropical Rainfall Measuring Mission (TRMM) Multi-Satellite Precipitation Analysis (TMPA) level 3B42 V7 product (Kummerow et al. 1998), and the 0.75° 2-m air temperature and humidity from the ECMWF Interim reanalysis (Dee et al. 2011). Detailed information about the model configuration and forcing fields can be found in Li et al. (2014).

The model is spun up from a state of rest for 30 years using monthly climatological forcing. Then HYCOM was integrated forward from March 1 2000 to December 31 2014 with the daily forcing fields described above. Note that the model was forced by CCMP winds from March 1 2000 to December 31 2010 and by ASCAT winds from January 1 2011 to December 31 2014. Earlier studies have shown that HYCOM is successful in representing the upper-ocean processes in the tropical Indian Ocean, including ISV of sea surface temperature (e.g., Li et al., 2013, 2014), sea surface salinity (Li et al. 2015) and SSH (Chen et al., 2015a). HYCOM is also able to well simulate the annual cycle and interannual variability of equatorial currents (Chen et al. 2015b) and eastern equatorial Indian Ocean upwelling (Chen et al., 2015a, 2016). As we shall see below, the wind-driven equatorial wave dynamics play an important role in generation of strong intraseasonal meridional currents in the southern BOB. Thus, we will further verify the HYCOM performance in simulating the ISV of equatorial currents by comparing with RAMA observations. The high correlation coefficients of 0.86 and 0.84 between intraseasonal zonal flow from RAMA moorings and from HYCOM solution averaged in the upper ocean at (0, 90°E) and (0, 80.5°E), together with their similar standard deviations (STDs) of 0.10 ms^{-1} versus 0.12 ms^{-1} and 0.11 ms^{-1} versus 0.13 ms^{-1} (Fig. 3), suggest that HYCOM reasonably captures both amplitude and phase of intraseasonal variability of equatorial zonal current. In section 3, we will also see that HYCOM successfully simulates the fundamental processes governing the eddy-like SSHAs, and thus is suitable for our investigation.

In this study, the ASCAT-forced run between 2011-2014 is used for our analysis and referred to as the HYCOM Main Run (MR). Besides MR, three additional experiments were performed for the 2011-2014 period with ASCAT wind forcing. To entirely exclude the forcing by atmospheric ISOs, in the NoISO experiment all of the atmospheric forcing fields are low-pass filtered with a 105-day Lanczos digital filter. The difference, *MR – NoISO*, hence measures the overall impact of ISO-related intraseasonal atmospheric forcing on the ocean. The third experiment, NoSTRESS, is performed with only the wind stress 105-day low-pass filtered. Hence the difference between MR and NoSTRESS quantifies the effect of intraseasonal wind stress associated with the ISOs through ocean dynamics.

To assess the relative importance of local wind forcing within the area of interest versus remote wind forcing outside the region, an additional experiment, named as NoLOCAL, is performed, in which the wind stress in the area of 84°E -100°E, 2°N -8°N (blue rectangle in Fig. 1) is 105-day low-pass filtered. Outside this rectangle area, there is a one-degree the transition zone (red dashed rectangle in Fig. 1), where the daily wind stress gradually changes to 105-day low-passed winds. The difference, *MR − NoLOCAL*, thus isolates the ISO-related local wind stress forcing effect, and NoLOCAL measures the remote forcing effect outside the box area. This experiment can help assess the relative importance of the local and coastal processes within the box and remote forcing from the equator. Output of the four experiments are all stored as 3-day mean data for the analysis period of 2011-2014.

3. Results

3.1. Observed Intraseasonal Meridional Currents

Figure 2 shows the daily time series of zonal current u and meridional current v observed by the SCSIO mooring from April 2013 to April 2014 over 20-145 m and 180-400 m depths (Section 1, Fig. 1). Evidently, u and v exhibit distinct characters in their variability. While u exhibits strong seasonal and semiannual variations, v is dominated by intraseasonal variability, with northward/southward flows alternating on intraseasonal timescales throughout the observation period and amplitude of ~0.4 m

s^{-1} above the main thermocline (~115 m for the climatological 20°C isotherm from ORAS4). The power spectra of the 20-145 m averaged *v* show strong spectral power at intraseasonal periods, with two distinct peaks at 38-day and 47-day periods (red line in Fig. 4a). The ISV is much stronger than the variability at lower frequencies (0-0.01 day^{-1}; > 100 days in period). The spectra of the 180-400 m averaged *v* also show significant power at intraseasonal periods, with peaks at 47days and 38days but with much weaker magnitudes (Fig. 4b). These results indicate that the observed *v* is associated with oceanic intraseasonal waves, with energy propagating downward from the surface as is clearly shown by the upward phase propagation of *v* (Fig. 2b). In comparison, the spectra of *u* have considerably weaker power at intraseasonal timescale of 30-50 days but stronger power at semiannual and annual frequencies (< 0.01 day^{-1}) in the upper layer and semiannual frequency in the deeper layer (Fig. 4, black curves). This means that the strong intraseasonal flow is a unique feature for *v* at the mooring site of ~5°N and worthy of in-depth investigation.

To better understand the current variability at the mooring site, we compare the OSCAR surface *v*, surface geostrophic current v_g from AVISO, and ADCP-measured *v* at 20 m and averaged between 20-145 m in Figure 5. During the observation period of the mooring, the three datasets are highly consistent. Interestingly, amplitudes and phases of the intraseasonal *v* (30-105 day band-pass filtered; Fig. 5b) are quite similar to those of the original daily *v* (Fig. 5a), confirming the dominance of ISV in the total meridional flow. The STDs of intraseasonal *v* from OSCAR, AVISO and mooring at

20 m are 0.18 m s^{-1}, 0.22 m s^{-1}, and 0.15 m s^{-1} during the mooring observed period, which are 81%, 76%, and 79% of the total daily v, respectively. Besides, the correlation coefficient between the daily v and intraseasonal v reaches 0.87, 0.81, and 0.88 for the three datasets. Note that the intraseasonal OSCAR v agrees well with the AVSIO v_g (Fig. 5b; r = 0.80). Therefore, the ISV is primarily contributed from the geostrophic component, and contribution from the Ekman flow is much less. The conclusion stands for 3°N-9°N in the eastern Indian Ocean (figure not shown). Consequently, we use AVISO SSH data to explore the spatial structure and temporal evolution~~s~~ of the observed current and sea level variability during the mooring observational period.

Time-longitude plot of intraseasonal SSHA along section 5°N suggests that the significant intraseasonal SSHA at the mooring site is mainly attributed to the westward propagation of Rossby waves with a phase speed of 0.20~0.71 m s^{-1} (Fig. 6a). Note that equatorial Yanai waves with “westward phase propagation” also exist at the 30-105 day periods and may still have appreciable magnitude near 5°N (e.g., Chatterjee et al. 2013). They however are antisymmetric about the equator and have eastward group velocity (Yanai and Maruyama 1966). As we shall see below (e.g., Fig. 10), it is primarily the westward propagating symmetric Rossby wave that contributes to the SSHAs here. Larger phase speeds tend to occur in boreal winter-spring due to the stronger oceanic stratification (Fousiya et al. 2015). For our composite analysis below, we use one STD of SSHA as the criterion for the selection of positive/negative

SSHA events at the mooring site, and the peaks of these events are labeled by white squares and green circles in Figure 6a. During the peaks of the high (low) SSHA events, the composite AVISO SSHA and OSCAR currents suggest that the mooring site is located roughly at the center of an anticyclonic (cyclonic) eddy-like structure (Figs 6b-6c). As these eddy-like structures propagate westward and pass the mooring, strong intraseasonal *v* is observed at the mooring site. In contrast, since the mooring site is roughly at the latitude of the eddy centers, the large zonal currents on the eddy edge is missed, and this is why we did not observe strong corresponding *u* at the mooring site (Figs 2a and 4). We further examine the time-latitude plot of intraseasonal SSHA along section 90.5°E (Fig. 6d), which confirms our discussion above, since the strong zonal gradients of positive/negative SSHA at ~5°N are associated with strong geostrophic meridional currents, with strong zonal currents occurring around 4°N and 6°N where strong meridional gradients of SSHA exist. Superimposed on the SSHA are meridional velocity vectors observed by the mooring from a depth of 20m (Fig. 6d). Larger amplitude *v* matches well with the boundaries between the positive and negative SSHA patches.

To understand whether or not the strong intraseasonal *v* is a unique situation of the mooring observational period, longer data records of OSCAR and AVISO at the mooring site are examined from 2011-2014. Figure 5 suggests that the geostrophic current remains the dominant component during 2011-2014. Besides, the mooring site is always passed by centers of eddy-like anomalies, as revealed by composite analysis using data from 2011-2014 (figure not shown). In fact, the mooring site is even affected by eddy-like currents in the annual climatology of 2001-2014 (Fig. 1). These results verify that the strong intraseasonal *v* at the mooring site near 5°N is a common feature. Due to the westward propagation of the eddy-like structures, we expect that strong intraseasonal *v* also exists west of the mooring. Power spectra of *u* and *v* verify our speculation (Fig. 7). Based on the daily AVISO geostrophic currents for 2011-2014, power spectra of zonal and meridional velocities at each grid point along 5°N are computed. Intraseasonal ~~component~~ with spectral peak of ~36 days dominates the meridional velocity, and the power peak extends westward from 94°E to 84°E (Fig. 7b). The wavelength is 1555 km corresponding to the phase speed of 0.5 m s^{-1} (Fig. 6a) and period of 36 days, which is consistent with wavelength of intraseasonal Rossby wave in the Pacific Ocean (Farrar, 2008). In comparison, the dominant zonal currents are at lower frequency with periods of longer than 100 day (Fig. 7a).

3.2. Wind forcing effects by the ISOs

To understand the causes for intraseasonal SSHA and thus intraseasonal meridional velocity, we choose a boxed area (3°N -7°N, 84°E -94°E~~; the black box~~ in Fig. 6b), which is centered at the mooring latitude of 5°N in the southern BOB, to form ~~the~~ time series. The STD of AVISO intraseasonal SSHA is 1.77 cm, which is approximately 50% of the STD of its climatological mean seasonal cycles of 3.78 cm. The simulated intraseasonal SSHA by HYCOM MR generally agrees with the observed SSHA (Fig.8a), with a correlation coefficient of 0.86 and a STD value of 1.80 cm during 2011-2014.

Given the success of HYCOM MR, results of other HYCOM experiments can be analyzed to understand the underlying physical processes. For example, in NoISO the forcing effects of atmospheric ISOs are removed, and therefore *MR – NoISO* measures the total forcing effect of ISOs. The intraseasonal SSHA from *MR – NoISO* agrees quite well with that in MR, showing a linear correlation coefficient of 0.93 (above 95% significance) (Fig. 8a). The STD of intraseasonal SSHA in *MR – NoISO* is 1.65 cm, which is also close to that in MR (1.80 cm). The good agreement between MR and *MR – NoISO* suggest that the observed SSH and current ISV~~s are~~ predominantly forced by atmospheric ISOs rather than induced by oceanic internal instabilities. By excluding intraseasonal wind stress forcing in NoSTRESS experiment, we further find that effect of atmospheric ISOs on SSHA is mainly through intraseasonal wind stress forcing (Fig. 8b), which affects SSHA through ocean dynamical processes rather than through surface buoyancy fluxes (heat and freshwater fluxes). The SSHA induced by surface wind stress (*MR-NoSTRESS*) has a comparable magnitude (1.58 cm) with that induced by total ISO forcing, and their correlation coefficient reaches 0.90.

Variability of SSH and upper-ocean circulation in the study region is affected by both local wind forcing and remote forcing of the equatorial zonal winds. To explore the effects of local versus remote wind stress forcing within and outside the southern BOB region (Fig. 1), we perform lagged correlation analyses between ASCAT intraseasonal zonal wind stress anomaly at each grid and AVISO intraseasonal SSHA averaged in the box shown in Figure 6b. The results demonstrate that intraseasonal SSHA in the southern BOB is significantly affected by zonal wind stress in the equatorial region (left column of Fig. 9). While positive correlation exceeds 0.6 from 80°E -90°E along the equator when wind stress leads by 25 days (black contour in Fig. 9a, top panel), negative correlation exceeds -0.4 in a similar region when wind stress leads by 0 or 5 days (Fig. 9a, two bottom panels). This result suggests that both eastern-boundary reflected and directly-forced Rossby waves are important in causing the observed SSHA at the mooring location, as further elaborated below.

Given that equatorial waves induce convergence and divergence along the Sumatra coast (Chen et al., 2016), we perform composite analyses with respect to SSHA along the Sumatra coast, labeled by the red box in Figure 10 with a width of one degree longitude off the coast between 5°S -5°N. The ±1STDs of SSHA averaged in the red box from ~~the~~ AVISO for the 2011-2014 period are ±3.16 cm, which are used to identify positive/negative SSHA events (Figure not shown). Based on this criterion, we identify 18 positive and 19 negative SSHA events. Due to their similar evolution ~~processes~~, we only show the composite results of positive SSHA events below. The days with SSHA maxima are taken as day 0. Then, SSHA composites from AVISO and currents from OSCAR for 15 days before (day -15) and 25 days after (day +25) day 0 are obtained (Fig. 10). To examine the sensitivity of results to the selection of the box, we also obtain the composite based on SSHA on the equator, similar to the analysis of Iskandar and McPhaden (2011) who used moored time series as an index, and obtain similar results. The composites of intraseasonal OLR and wind stress anomalies in the tropical Indian Ocean corresponding to the positive SSHA events are presented in Fig. 11.

Intraseasonal westerly wind anomalies in the equatorial Indian Ocean (arrows of Fig. 11; -15 day), which are associated with strong intraseasonal atmospheric convection (active phase of the ISOs; blue shading in Fig. 11) cause equatorial Ekman convergence, increasing SSHA and eastward flows along the equator (Fig. 10). The positive SSHA signals first propagate eastward along the equator as equatorial Kelvin waves. Upon arriving at the eastern boundary, part of the energy propagates northward along the coast of Sumatra as coastal Kelvin waves, and subsequently radiates westward as long Rossby waves with eddy-like structures centered at 5°N, increasing SSHA at the mooring location after 20-25 days (+5 day and +10 day in Fig. 10). Meanwhile, intraseasonal easterly wind anomalies occupy the equatorial Indian Ocean (+5 day in Fig. 11), inducing cyclonic eddy-like structures around the mooring location after another 20-25 days (Fig. 10; see also Fig. 16 below). These explain the lagged correlation shown Fig. 9a and the alternating meridional currents observed by the mooring. Note that in the equatorial Indian Ocean, the propagating first meridional mode Rossby waves associated with the first baroclinic mode exist when the period is longer than ~30days, and those associated with the second baroclinic mode exist when the period is longer than ~40days (see Fig. 12 of Han 2005). Consequently, the observed 38-day spectral peak of *v* (Fig. 4a) is largely contributed from the Rossby waves associated with the first baroclinic mode and the 47-day peak, from both the first and second baroclinic modes.

Accompanying the equatorial Ekman convergence and positive SSHA, there ~~are~~ off-equatorial Ekman divergence and therefore negative SSHA on both sides of the equator (Fig. 10). This is the typical structure of the first meridional mode Rossby wave that is directly driven by zonal wind stress over the eastern equatorial basin (see also Nagura and McPhaden 2014 for directly forced Rossby waves). These directly forced Rossby waves explain the negative correlation with 0~5 day lead of zonal wind stress in the eastern equatorial basin (Fig. 9a, two bottom panels).

In addition to zonal wind stress in the equatorial basin, Ekman pumping associated with local wind stress curl over the southern BOB can also affect SSHA there, which is also mentioned by previous studies (e.g., Iskandar and McPhaden 2011; Nagura and McPhaden 2010). Indeed, SSHA in the southern BOB is negatively correlated with the local Ekman pumping velocity anomaly with correlation coefficients exceeding -0.4 with 0~5 day lead by Ekman pumping velocity (Fig. 9b). This is because positive (negative) Ekman pumping velocity associated with positive (negative) wind stress curl anomaly shoals (deepens) the thermocline and reduces (increases) SSHA. The SSHA signals can propagate westward as Rossby waves, affecting the SSHA in the western Bay. Note that propagating Rossby waves exist at 5°N on intraseasonal periods, because the critical latitudes (McCreary et al., 1986) of intraseasonal Rossby waves associated with the first baroclinic mode are higher than 5°N. The critical latitude θ_c is defined as $\tan(\theta_c) = \frac{c}{2\omega R}$, where c is baroclinic mode speed, R is the earth's radius, ω is the frequency with $\omega = \frac{2\pi}{T}$ and T is the period. Based on the density profile from ORAS4 data, we estimate the theoretical Kelvin wave phase speed of the first baroclinic mode speed being 3.05 ms^{-1} in our region of interest. For T=36 days, which is close to the lower bound of intraseasonal periods (Fig. 4a), θ_c =6.8°N. In comparison, the second baroclinic mode with phase speed of 1.52 ms^{-1} can affect 47 day variability on the equator but not at 5°N since its θ_c is less than 5°N.

To provide quantitative estimates for the effects of remote versus local wind forcing, we trace the SSHA signals along the route composed by the eastward route along the equator, the northwestward route along the Sumatra coast, and the westward route at 5°N meridian (the route A-B-C-D with longitudes of 80°E, 98.5°E, 95°E, and 80°E shown by the red line in the bottom panel of Fig. 9a). Figure 13 shows the time-distance plots of intraseasonal SSHA from AVISO, HYCOM MR, HYCOM NoLOCAL (assessing the remote forcing effect outside the Fig. 1 boxed region), and *MR – NoLOCAL* (assessing local wind forcing effect within the box). Both AVISO and HYCOM MR show clear propagation from A-B-C with faster speed and from C-D with slower speed (Figs 13a-13b). It takes 10.4 (20.7) days for the first (second) baroclinic mode Kelvin waves to propagate from A to C, and another 5.4 days for the first baroclinic mode Rossby wave from C to the mooring site. Indeed, the travel time of the observed and simulated SSHA signals from A to C indicates a mixed behavior of first and second baroclinic modes. Wind forcing may also obscure pure free Rossby wave phase speeds, leading to the slower speeds than expected for free wave propagation. In NoLOCAL, the SSHAs present similar features and magnitudes to those in HYCOM MR and AVISO observation, suggesting that remote winds outside the boxed region play an important role in affecting the intraseasonal SSHA in the southern BOB (Fig. 13c). Composite intraseasonal SSHA and surface currents from NoLOCAL further verify the dominant role of remote, equatorial forcing (Fig. 12). In comparison, in *MR – NoLOCAL*, the SSHAs are visibly weaker (Fig. 13d). Interestingly, the intensity of locally generated SSHA shows obvious interannual variation. As a result, local wind forcing also makes significant contributions to strong SSHAs in some years, which also propagate westward (Fig. 13d).

To better quantify the remote versus local wind forcing effects, in Figure 8c we compare the box-average intraseasonal SSHA time series from MR, NoLOCAL, and *MR - LOCAL*. Overall, remote wind forcing dominates the total SSHA ~~in most of the cases~~. The correlation coefficient between MR and NoLOCAL is 0.82, while that between MR and *MR – NoLOCAL* is 0.46. The STDs of intraseasonal SSHA are 1.61 and 1.03 cm in NoLOCAL and *MR - NoLOCAL* accouting for 89% and 57% of the total SSHA in MR~~, respectively~~. Albeit with smaller amplitude and correlation, local wind forcing effect ~~is~~ also considerable, particularly for some strong SSHA events. Specifically, both remote and local forcing effects contribute to the SSHA in July 2011, May 2013, and December 2014 (red arrows in Fig. 8c), whereas they have opposite effects on SSHAs of January 2011, August 2011 and July-August 2014 (blue arrows). We therefore ~~come to the conclusion~~ that the observed ISV~~s~~ in SSH and meridional current ~~are~~ primarily induced by remote forcing of the equatorial winds through both reflected and directly forced Rossby waves, and secondarily through local forcing of wind stress curl anomalies near 5°N.

3.3. Symmetric Equatorial Rossby Waves

Besides the eddy-like SSHAs near 5°N, eddy-like SSHAs can also be seen south of the equator from day +10 to day +25 (Fig. 10), ~~also~~ propagating westward along 5°S~~,~~ but with smaller amplitudes. The rough symmetric signals about the equator, with in-phase SSHAs on both side of the equator, resemble the structure of the equatorially symmetric waves. The equatorially symmetric structure, with positive SSHAs off the equator and weakly negative SSHA on the equator, is the typical structure of the first meridional mode Rossby waves. Due to the slanted eastern boundary in the EIO, however, Rossby waves are not "purely symmetric" (Han et al., 2011), and there are contributions from anti-symmetric components.

To understand the components of the observed ISVs, we perform a meridional decomposition to the intraseasonal observed SSHA to Kelvin wave mode D_0 and

Rossby wave modes $D_{n+1}+(n+1)D_{n-1}$ in the form of $h=h_0D_0+\sum_{n=1}^{\infty}h_n(D_{n+1}+(n+1)D_{n-1})$, where parabolic cylinder functions $D_n(y')$ can be represented in terms of the Hermite Polynomial $H_n(y')$ as $D_n(y')=\frac{e^{-y'^2/4}}{\sqrt{n!\sqrt{2\pi}}}H_n(y')$ (Zheng et al., 1995). Herein, $y'=y\sqrt{2\beta/c}$ is non-dimensional meridional coordinate, where $c=\sqrt{g'H}$ is the phase speed of baroclinic mode inertial wave in a 1.5 layer ocean model, g' is the reduced gravity parameter, and H is the mean upper layer thickness of the 1.5-layer model. β is defined by $\beta=2\Omega\cos\theta/r_0$, where Ω is the rotation rate of earth, θ is the latitude, and r_0 is the earth radius. $H_n(y')$ are derived from $e^{-y'^2/2}H_n(y')=(-\frac{d}{dy'})^n e^{-y'^2/2}$. More details can be found in White and Tai (1992) and Zheng et al. (1995).

Three profiles, at 85°E, 90.5°E, and 93°E, are chosen to represent the different areas of the EIO. Based on the AVISO SSHA composites shown in Figure 10, we expand SSHAs along the three profiles on -5, +10, and +25 days to understand their features in different stages. Overall, the AVISO SSHAs (grey dots in Fig. 14) can be well represented by the sum of the Kelvin wave mode and the first two meridional modes Rossby wave (red lines in Fig. 14). On -5 day when Kelvin waves dominate the equatorial area, the Kelvin wave mode and the first meridional mode symmetric Rossby wave (red dashed line in Fig. 14) control the meridional distribution of SSHA. In comparison, the second meridional mode anti-symmetric Rossby wave (blue lines in Fig. 14) contributes less to SSHA. On +10 day when the reflected Rossby waves starting to appear, the first meridional mode symmetric wave induces equatorial symmetric SSHA along 93°E, with peaks around 5°N and 5°S. At the same time, the second meridional mode anti-symmetric Rossby wave leads to high SSHA around 5°N but low SSHA around 5°S. As a result, SSHA along 93°E presents significantly asymmetrical feature around the equator with high SSHA in the northern part. The asymmetrical Rossby waves propagate westward and arrive at 85°E on +25 day (Fig. 10), where SSHA are still contributed from the first three modes (Fig. 14). In comparison, because the high SSHA event has passed by and no new one arrives, the SSHA along 90°E on +25 day tends to be symmetric and dominated by symmetric wave modes (Fig. 14). Due to generation of another low SSHA event (Fig. 10), the SSHA along 93°E on +25 day becomes asymmetric again, and the anti-symmetric modes contribute substantially to the SSHA meridional distribution (Fig. 14).

The decomposition of SSHA into meridional modes supports the observations and model results, showing that the sum of Kelvin wave mode and first two meridional mode Rossby waves reproduce the observed SSHA well in the equatorial Indian Ocean. The first meridional mode Rossby wave dominates the solution near 5°N, and the second meridional mode contributes to the asymmetric component about the equator. Strong ISV of meridional velocity at 5°N is part of the eddy like structures associated with the Rossby waves, whose natural modes ensure peaks around this latitude (Fig. 14). The Kelvin wave mode is indispensable to the solution within ~~the~~ equatorial Rossby radius, but it tends to weaken the effects of Rossby waves and contributes less to the eddy-like SSHAs.

4. Summary and Discussion

In response to the strong wind forcing of atmosphere ISOs, zonal currents in the eastern equatorial Indian Ocean exhibit pronounced intraseasonal variability, which has been intensively investigated by many studies (e.g., Han et al. 2001; Iskandar and McPhaden 2011; Nagura and McPhaden 2012). In comparison, there are far fewer studies for the intraseasonal variability in meridional currents. The SCSIO deployed a subsurface mooring at 5ºN, 90.5ºE (Fig. 1). The one-year records of the ADCPs reveal pronounced ISV in the meridional current, which is characterized and explained in this study.

In the ADCP measurements of the mooring there are strong intraseasonal meridional currents with an amplitude of 0.4 m s^{-1} and a typical period of 30-50 days in the upper 150 m (Fig. 2). They are by far larger in magnitude than the mean flow and seasonal cycle of *v*. Such prominent ISV is however not seen in zonal current *u*. Further analysis shows that those anomalous meridional currents are primarily geostrophic and closely associated with frequently occurring eddy-like SSHAs centered near 5ºN (Fig. 6). These eddy-like SSHAs propagate westward, causing pronounced ISV of upper-ocean *v* not only at the mooring site but also the entire southern BOB between 84°-94°E (Fig. 7). Since most of the eddy-like SSHAs are centered near 5°N, there is no significant ISV in zonal current observed by the mooring. To the southeast of the Sri Lanka island, the SSHAs are considerably weakened, while some intraseasonal SSHAs are generated locally (Fig. 6a). In addition to local wind forcing, the strong ocean internal instabilities off Sri Lanka (Chen et al., 2012; Sengupta et al., 2001) should contribute to generating these local SSHA signals. Short Rossby waves with eastward energy propagation may occur around southeast of Sri Lanka, but have no visible influence on SSHA and currents at the mooring site before they are severely damped by mixing due to their slow eastward group velocity and short wavelengths (not shown).

Further analysis of observational data and HYCOM experiments demonstrate that the observed eddy-like SSHAs at 5°N are predominantly caused by remote equatorial wind stress forcing associated with atmospheric ISOs, through directly forced and eastern-boundary reflected Rossby waves. The equatorial westerly (easterly) wind stress anomalies directly force symmetric Rossby waves with negative (positive) SSHA around 5°N and 5°S. Meanwhile, intraseasonal equatorial zonal wind stress excites equatorial Kelvin waves, which propagate eastward to the Sumatra coast, and subsequently reflect back into the ocean interior as westward propagating Rossby waves, contributing to the eddy-like SSHAs at the mooring location (Figs 10 and 13). Similar processes also have been shown at seasonal and interannual scales (McCreary and Yu, 1992*;* Shankar et al., 2002; Vinayachandran et al., 2002). Compared to remote forcing, local wind stress forcing in the southern BOB is less important, but it also contributes significantly to some strong SSHA events through local Ekman pumping and ~~generating~~ westward propagating Rossby waves, such as those occurred in July 2011, May 2013, and December 2014 (Fig. 8c).

Based on the statistics for the intraseasonal SSHAs near the Sumatra coast, there are 19 events occurred in November-April and 18 events in May-October. No evident seasonal preference is detected in terms of event number. It is likely that both the winter MJO and the summer monsoon ISO (e.g., Yasunari, 1980; Krishnamurti and Subrahmanyam, 1982) can cause the strong ISVs in SSH and meridional current at 5°N. Based on the real-time multivariate MJO (RMM) index (Wheeler and Hendon 2004), we identify significant MJO variance with the ~~RMM~~ amplitude large than 1.5, and then obtain the composite intraseasonal OLR and wind stress maps for the eight MJO phases (Fig. 15). Strong wind stress anomalies are seen in the equatorial Indian Ocean. For example, westerly winds are seen near the equator at phase 3-4, while easterly winds are seen at phase 7-8. These surface wind anomalies, together with their accompanied off-equatorial wind stress curls, are the primary driver of the observed SSH and meridional current ISV at 5ºN in November-April, as has been demonstrated in our analysis. On the other hand, the wind anomalies of the summer monsoon ISO are dramatically different in spatial-temporal characteristics from those of the MJO. Therefore, the two dominant mode of ISOs may induce varied ocean current ISV~~s~~ in strength, spatial distribution, and even mechanisms, which is an interesting theme for future studies.

The eddy-like structures, in essence, are ~~parts of~~ equatorial ~~symmetric~~ waves. Overall, the meridional structures of SSHA in the eastern equatorial Indian Ocean can be well represented by the sum of the Kelvin wave mode and the first two meridional mode~~s~~ ~~of~~ Rossby waves (Fig. 14). While the first meridional mode Rossby wave dominates the meridional structure of SSHA overall, the second meridional mode anti-symmetric Rossby wave contributes to the SSHA particularly in the eddy-like regions near 5°N and 5°S (Figs 10 and 14). In general, the intraseasonal SSHAs and meridional currents are stronger north of the equator than in the South, which is primarily due to inclined coastline of the eastern boundary that affects the Kelvin wave reflection (Fig. 10; Han et al., 2011).

The eddy-like Rossby wave signals can have a significant impact on the upper-ocean circulation in the eastern equatorial Indian Ocean, particularly in the southern BOB. Due to dissipation and modification by local winds, the Rossby waves are greatly attenuated in the western basin; but their associated equatorial zonal flow remains considerable in magnitude (Fig. 16). At ~~the equatorial~~ 60°E, the related intraseasonal zonal currents averaged at the upper 30 m can reach 0.2 m s^{-1} ~~on~~ +50 day of the composite, which may significantly impact on intraseasonal variability of upper ocean currents, such as the Wyrtki jets, over the equatorial Indian Ocean.

Acknowledgements

The AVISO data were obtained at http://www.aviso.altimetry.fr/en/data/data-access.html, the OSCAR data at ftp://podaac-ftp.jpl.nasa.gov/allData/oscar/preview/L4/oscar_third_deg, the ASCAT data at http://apdrc.soest.hawaii.edu:80/dods/public_data/satellite_product/ASCAT/daily, and the ORAS4 data at http://apdrc.soest.hawaii.edu:80/dods/public_data/Reanalysis_Data/ORAS4. The processed mooring data used to construct figures in this work are also available, and anyone who wants to get access to these data could contact the corresponding author, Dongxiao Wang (dxwang@scsio.ac.cn). G. Chen and D. Wang are supported by NSFC 41476011, NSFC 41521005, XDA11010103, and Youth Innovation Promotion Association CAS (2017397). W. Han and Y. Li are supported by NSF AGS 1446480, NSF OCE 1558736 and NMMD SSC-03-002. This is PMEL contribution no. 4591.

References

Atlas, R., J. Ardizzone, and R. N. Hoffman, 2008: Application of satellite surface wind data to ocean wind analysis. P Soc Photo-Opt Ins, 7087 , doi:10.1117/12.795371

Balmaseda, M. A., K. Mogensen, and A. T. Weaver, 2013: Evaluation of the ECMWF ocean reanalysis system ORAS4. Q J Roy Meteor Soc, 139**,** 1132-1161.

Bonjean, F., and G. S. E. Lagerloef, 2002: Diagnostic model and analysis of the surface currents in the tropical Pacific Ocean. J Phys Oceanogr, 32, 2938-2954.

Bentamy, A., and D. Croize-Fillon, 2012: Gridded surface wind fields from Metop/ASCAT measurements, *International Journal of Remote Sensing*, 33, 1729-1754.

Chatterjee, A., D. Shankar, J. McCreary, and P. Vinayachandran (2013), Yanai Waves in the Western Equatorial Indian Ocean, *Journal of Geophysical Research: Oceans*, *118*, 1206–1210, doi:1210.1002/jgrc.20104.

Chelton, D. B., M. G. Schlax, J. M. Lyman, and G. C. Johnson, 2003: Equatorially trapped Rossby waves in the presence of meridionally sheared baroclinic flow in the Pacific Ocean. Prog Oceanogr, 56, 323-380.

Chen, G., D. Wang, and Y. Hou, 2012: The Features and interannual variability mechanism of mesoscale eddies in the Bay of Bengal. Continental Shelf Research, 47, 178-185.

Chen, G. X., W. Q. Han, Y. L. Li, D. X. Wang, and T. Shinoda, 2015a: Intraseasonal variability of upwelling in the equatorial Eastern Indian Ocean. J Geophys Res-Oceans, 120, 7598-7615.

Chen, G., W. Han, Y. Li, D. Wang, and M. J. McPhaden, 2015b: Seasonal-to-Interannual Time Scale Dynamics of the Equatorial Undercurrent in the Indian Ocean. J Phys Oceanogr, 45, 1532-1553.

Chen, G., W. Han, Y. Li, and D. Wang, 2016: Interannual Variability of Equatorial Eastern Indian Ocean Upwelling: Local versus Remote Forcing, J Phys Oceanogr, 46, 789–807.

Cheng, X. H., S. P. Xie, J. P. McCreary, Y. Q. Qi, and Y. Du, 2013: Intraseasonal variability of sea surface height in the Bay of Bengal. J Geophys Res-Oceans, 118, 816-830.

Dee, D. P., and Coauthors, 2011: The ERA-Interim reanalysis: configuration and performance of the data assimilation system. Q J Roy Meteor Soc, 137**,** 553-597.

Ducet, N., P. Y. Le Traon, and G. Reverdin, 2000: Global high-resolution mapping of ocean circulation from TOPEX/Poseidon and ERS-1 and-2. J Geophys Res-Oceans, 105, 19477-19498.

Durland, T. S., R. M. Samelson, D. B. Chelton, and R. A. de Szoeke, 2011: Modification of Long Equatorial Rossby Wave Phase Speeds by Zonal Currents. J Phys Oceanogr, 41, 1077-1101.

Farrar, J.T., 2008: Observations of the dispersion characteristics and meridional sea level structure of equatorial waves in the Pacific Ocean. J Phys Oceanogr, 38(8), 1669-1689.

Fousiya, T., A. Parekh, C. Gnanaseelan, 2015: Interannual variability of upper ocean stratification in Bay of Bengal: observational and modeling aspects, Theor Appl Climatol, doi:10.1007/s00704-015-1574-z.

Girishkumar, M. S., M. Ravichandran, and M. J. McPhaden, 2013: Temperature inversions and their influence on the mixed layer heat budget during the winters of 2006-2007 and 2007-2008 in the Bay of Bengal. J Geophys Res-Oceans, 118, 2426-2437.

Han, W. Q., D. M. Lawrence, and P. J. Webster, 2001: Dynamical response of equatorial Indian Ocean to intraseasonal winds: zonal flow. Geophys Res Lett, 28, 4215-4218.

Han, W., 2005: Origins and Dynamics of the 90-Day and 30–60-Day Variations in the Equatorial Indian Ocean. J Phys Oceanogr, 35, 708-728.

Halkides, D.J., W. Han, T. Lee and Y. Masumoto, 2007: Effects of sub-seasonal variability on seasonal-to-interannual Indian Ocean meridional heat transport. Geophys. Res. Lett., 34, L12605, doi:10.1029/2007GL030150.

Hendon, H. H., and J. Glick, 1997: Intraseasonal air-sea interaction in the tropical Indian and Pacific Oceans. J Climate, 10, 647-661.

Iskandar, I., W. Mardiansyah, Y. Masumoto, and T. Yamagata, 2005: Intraseasonal Kelvin waves along the southern coast of Sumatra and Java. J Geophys Res-Oceans, 110.

Iskandar, I., and M. J. McPhaden, 2011: Dynamics of wind‐forced intraseasonal zonal current variations in the equatorial Indian Ocean, J. Geophys. Res., 116, C06019, doi:10.1029/2010JC006864.

Izumo, T., and Coauthors, 2010: Influence of the state of the Indian Ocean dipole on the following year's El Niño. Nat Geosci, 3, 168–172.

Johnson, E. S., F. Bonjean, G. S. E. Lagerloef, J. T. Gunn, and G. T. Mitchum, 2007: Validation and error analysis of OSCAR sea surface currents. J Atmos Ocean Tech, 24, 688-701.

Krishnamurti, T. N., and D. Subrahmanyam (1982), The 30-50 day mode at 850 mb during MONEX, *J. Atmos. Sci.*, *39*(9), 2088-2095.

Kummerow, C., W. Barnes, T. Kozu, J. Shiue, and J. Simpson, 1998: The Tropical Rainfall Measuring Mission (TRMM) sensor package. J Atmos Ocean Tech, 15**,** 809-817.

Le Traon, P. Y., F. Nadal, and N. Ducet, 1998: An improved mapping method of multisatellite altimeter data. J Atmos Ocean Tech, 15, 522-534.

Li, Y., W. Han, T. Shinoda, C. Wang, R. C. Lien, J. N. Moum, and J. W. Wang, 2013: Effects of the diurnal cycle in solar radiation on the tropical Indian Ocean mixed layer variability during wintertime Madden-Julian Oscillations. J Geophys Res, **118,** 4945-4964, doi:4910.1002/jgrc.20395.

Li, Y. L., W. Han, T. Shinoda, C. Z. Wang, M. Ravichandran, and J. W. Wang, 2014:

Revisiting the Wintertime Intraseasonal SST Variability in the Tropical South Indian Ocean: Impact of the Ocean Interannual Variation. J Phys Oceanogr, 44**,** 1886-1907.

Li, Y., W. Han, and T. Lee, 2015: Intraseasonal sea surface salinity variability in the equatorial Indo‐Pacific Ocean induced by Madden‐Julian oscillations. J Geophys Res, 120**,** 2233-2258.

Lutjeharms, J. R. E., N. D. Bang, and C. P. Duncan, 1981: Characteristics of the current east and south of Madagascar. Deep Sea Res., 28, 879-899.

Madden, R. A., and P. R. Julian, 1971: Detection of a 40-50 day oscillation in the zonal wind in the tropical Pacific. J Atmos Sci, 28, 702-708.

Masumoto, Y., H. Hase, Y. Kuroda, H. Matsuura, and K. Takeuchi, 2005: Intraseasonal variability in the upper layer currents observed in the eastern equatorial Indian Ocean. Geophys Res Lett, 32.

Matsuno, T., 1966: Quasi-geostrophic motions in the equatorial area. Journal of the Meteorological Society of Japan, 44, 25–43.

Mamayev, O., 1975: Temperature-salinity analysis of world ocean waters. *Elsevier oceanography series***,** Amsterdam, 374 pp.

McCreary, J.P. and Z. Yu, (1992): Equatorial dynamics in a 212-layer model. Progress in Oceanography, 29(1), 61-132.

McPhaden, M. J., 1982: Variability in the Central Equatorial Indian-Ocean .1. Ocean Dynamics. J Mar Res, 40, 157-176.

McPhaden, M. J., and Coauthors, 2009: RAMA: The Research Moored Array for African–Asian–Australian Monsoon Analysis and Prediction. Bull. Amer. Meteor. Soc., 90, 459–480, doi:10.1175/2008BAMS2608.

Moore, D.W., 1968. Planetary waves in an equatorial ocean. Ph.D. thesis, Harvard University, Cambridge, MA, 207pp.

Nagura, M., and M. J. McPhaden, 2012: The dynamics of wind-driven intraseasonal variability in the equatorial Indian Ocean, J. Geophys. Res., 117, C02001, doi:10.1029/2011JC007405.

Nagura, M., and M. J. McPhaden, 2014: Zonal momentum budget along the equator in the Indian Ocean from a high-resolution ocean general circulation model. J. Geophys. Res., 119, 4444–4461.

Ogata, T., H. Sasaki, V. S. N. Murty, M. S. S. Sarma, and Y. Masumoto, 2008: Intraseasonal meridional current variability in the eastern equatorial Indian Ocean. J Geophys Res-Oceans, 113.

Pujiana, K., A. L. Gordon, and J. Sprintall, 2013: Intraseasonal Kelvin wave in Makassar Strait. J Geophys Res-Oceans, 118, 2023-2034.

Qiu, B., M. Mao, and Y. Kashino, 1999: Intraseasonal variability in the indo-pacific throughflow and the regions surrounding the Indonesian seas. J Phys Oceanogr, 29, 1599-1618.

Reppin, J., F. A. Schott, J. Fischer, and D. Quadfasel, 1999: Equatorial currents and transports in the upper central Indian Ocean: Annual cycle and interannual variability. J Geophys Res-Oceans, 104, 15495-15514.

Schiller, A., S. E. Wijffels, J. Sprintall, R. Molcard, and P. R. Oke, 2010: Pathways of intraseasonal variability in the Indonesian Throughflow region. Dynam Atmos Oceans, 50, 174-200.

Schott, F., and D. R. Quadfasel,1982: Variability of the Somali Current system during the onset of the southwest monsoon, 1979. J Phys Oceanogr, 12, 1343-1357.

Schott, F. A., and J. P. McCreary, 2001: The monsoon circulation of the Indian Ocean. Prog Oceanogr, 51, 1-123.

Sengupta, D., R. Senan, and B. N. Goswami, 2001: Origin of intraseasonal variability of circulation in the tropical central Indian Ocean. Geophys Res Lett, 28, 1267-1270.

Shankar, D., P.N. Vinayachandran, and A.S. Unnikrishnan, 2002: The monsoon currents in the north Indian Ocean. Progress in oceanography, 52(1),63-120.

Shetye, S.R., A.D. Gouveia, S.S.C. Shenoi, D. Sundar, G.S. Michael, and G. Nampoothori, 1993: The western boundary current of the seasonal subtropical gyre in the Bay of Bengal. J Geophys Res, 98, 945-954.

Shinoda, T., T. Jensen, M. Flautau and S. Chen, 2013: Surface wind and upper ocean variability associated with the Madden-Julian Oscillation simulated by the Coupled Ocean/Atmosphere Mesoscale Prediction System (COAMPS). Mon Wea Rev, 141, 2290-2307.

Vinayachandran P. N. and J. Kurian, 2007: Hydrographic observations and model simulations of the Bay of Bengal freshwater plume. Deep Sea Res I, 54, doi:10.1016/j.dsr.2007.01.007.

Vinayachandran, P. N., D. Shankar, S. Vernekar, K. K. Sandeep, P. Amol, C. P. Neema, and A. Chatterjee, 2013: A summer monsoon pump to keep the Bay of Bengal salty. Geophys Res Lett, 40 (9), 1777-1782.

Vinayachandran, P.N., S. Iizuka, and T. Yamagata, 2002: Indian Ocean dipole mode events in an ocean general circulation model. Deep Sea Research Part II: Topical Studies in Oceanography, 49(7),1573-1596.

Wallcraft, A., E. Metzger, and S. Carroll, 2009: Software Design Description for the HYbrid Coordinate Ocean Model (HYCOM), Version 2.2.

Webster, P. J., and Coauthors, 2002: The jasmine pilot study. B Am Meteorol Soc, 83, 1603-1630.

White, W. B., and C. Tai, 1992: Reflection of Interannual Rossby Waves at the Maritime Western Boundary of the Tropical Pacific. J Geophys Res, 97(C9), 14305-14322.

Wielicki, B. A., B. R. Barkstrom, E. F. Harrison, R. B. Lee, G. L. Smith, and J. E. Cooper, 1996: Clouds and the earth's radiant energy system (CERES): An earth observing system experiment. B Am Meteorol Soc, 77, 853-868.

Yanai, M., and Y. Hayashi, 1969: Large-scale equatorial waves penetrating from the upper troposphere into the lower stratosphere. J. Meteor. Soc. Japan, 47, 167–182.

Yasunari, T. (1980), A quasi-stationary appearance of 30 to 40 day period in the cloudiness fluctuations during the summer monsoon over India, *J. Meteor. Soc. Japan*, *58*, 225-229.

You, Y., and M. Tomczak, 1993: Thermocline circulation and ventilation in the Indian Ocean derived from water mass analysis. Deep-Sea Res., Part I, 40**,** 13-56.

Zheng, Q. N., X. H. Yan, C. R. Ho, and C. K. Tai, 1995: Observation of Equatorially Trapped Waves in the Pacific Using Geosat Altimeter Data, Deep-Sea Res Pt I, 42(5), 797-817.

Figure Captions

Figure 1. The annual climatology of surface currents (vector; m s^{-1}) from OSCAR during 2001-2014. The red star denotes the mooring location. The blue solid rectangle marks the region of 2°N-8°N, 84°E-100°E, where wind stress forcing is 105-day low-pass filtered in the NoLOCAL experiment (Section 2). The area between blue solid rectangle and red dashed rectangle is the transient zone, where the daily wind stress outside the box gradually transits to the 105-day low-pass filtered forcing inside the box.

Figure 2. Mooring-observed daily (a) zonal current *u* and (b) meridional current *v* (m s^{-1}) of the upper 400 m at 5ºN, 90.5ºE from April 2, 2013 through April 15, 2014. The black line marks 0 velocity contour.

Figure 3. (a) Time series of 40-200 m averaged intraseasonal zonal currents (30-105 day band-pass filtered) at 0, 90°E from RAMA (black line) and HYCOM (red line). (b) Same as (a) but for 25-180 m at 0, 80.5°E.

Figure 4. The power spectrum of *u* (black) and *v* (red) averaged over (a) 20-145 m and (b) 180-400 m observed by the mooring at 5ºN, 90.5ºE.

Figure 5. (a) Daily time series of the surface *v* from OSCAR product (black) and surface geostrophic meridional current from AVISO (red) during January 2011-December 2014, and 20 m (blue) and 20-145 m averaged (dashed-pink) *v* from the mooring measurements during April 2013- April 2014, at 5ºN, 90.5ºE. (b) Same as (a) but for the 30-105 day band-pass filtered currents.

Figure 6. (a) Time-longitude plot of intraseasonal SSHA along 5°N during April 2013-April 2014. White squares and green circles denote peaks of positive and negative SSHA events at the mooring site (5°N, 90.5°E) exceeding one STD magnitude. (b) Intraseasonal SSHA and currents for the composite of the positive SSHA events. The black box shows the region covers the 3°N-7°N, 84°E-94°E. (c) Same as (b) but for the negative SSHA events. (d) Time-latitude plot of intraseasonal SSHA at 90.5°E. Superimposed on the SSHA are velocity vectors observed by the mooring at 5°N, 90.5°E from a depth of 20 m.

Figure 7. Power spectra of (a) *u* and (b) *v* along 5°N based on daily AVISO surface geostrophic current. The black dashed line in (b) denotes the peak at 36 day period.

Figure 8. (a) Time series of intraseasonal (30-105 day band-pass filtered) SSHA averaged in the 3°N-7°N, 84°E-94°E (black box in Fig. 6b) from the AVISO, HYCOM MR and the solution difference, *MR-NoISO* (measuring the total ISO forcing effect) for 2011-2014. (b) Same as (a) but from the MR, *MR-NoISO*, and *MR-NoSTRESS* (measuring wind stress effect). (c) Same as (a) but from MR, NoLOCAL (measuring remote forcing effect), and *MR-NoLOCAL* (blue line; measuring local forcing effect).

Figure 9. (a) Correlation coefficients between intraseasonal ASCAT zonal wind stress τ^x at each grid point and intraseasonal AVISO SSHA averaged over 3°N-7°N, 84°E-94°E (black box in Fig. 6b) when τ^x leads SSHA by 25, 20, 15, 10, 5, and 0 days. The black (white) contours represent 0.6 (±0.4) correlations. Correlation values below 95% significance level are masked white. (b) Same as (a) but for the correlations

between intraseasonal Ekman pumping velocity W_E and box-averaged SSHA. The red lines in (a) denote routes along the equator (from A to B), along the coasts of Sumatra (B-C), and along 5°N (C-D). Longitudes of A-D are 80°E, 98.5°E, 95°E, and 80°E, respectively.

Figure 10. Composite intraseasonal AVISO SSHA (color; cm) and intraseasonal OSCAR currents (vectors; m s^{-1}) of the positive SSHA events during 2011-2014, with a 5-day interval. The 0 day is defined by the SSHA maximum along the Sumatra coast (within one-longitude of the Sumatra coast between 0°-5°N, shown in the -15 day map). The high SSHA events are identified with a criterion of SSHA exceeding the STD value.

Figure 11. Composite intraseasonal (30-105 day filtered) OLR anomaly (color) and intraseasonal wind stress anomaly (vectors) in the tropical Indian Ocean corresponding to the positive SSHA events during 2011-2014.

Figure 12. Same as Figure 10 but based on NoLOCAL experiment.

Figure 13. (a) Time-longitude plots of intraseasonal (30-105 day band-pass filtered) SSHA from AVISO along the red lines shown in Figure 9a. (b)-(d) are the same as (a) but for SSHA from (b) the MR, (c) the NoLOCAL experiment measuring the remote wind forcing effect, and (d) their difference *MR- NoLOCAL* that assesses the local forcing effect.

Figure 14. Meridional distributions of intraseasonal SSHA along 85°E, 90.5°E and 93°E on -5 day, +10 day and +25 day. Grey dots are the composite SSHAs shown in

Figure 10. Red solid, red dashed, cyan, black, and blue curves are superposition of the first three meridional modes, superposition of the first two meridional modes, the Kelvin wave meridional mode, the first meridional symmetric Rossby wave mode, and the second meridional anti-symmetric Rossby wave mode, respectively.

Figure 15. Composite intraseasonal wind stress anomaly (vectors) and OLR anomaly (color) for eight phases of the RMM index.

Figure 16. Same as Figure 10 but for the tropical Indian Ocean from +25 day to +60 day.

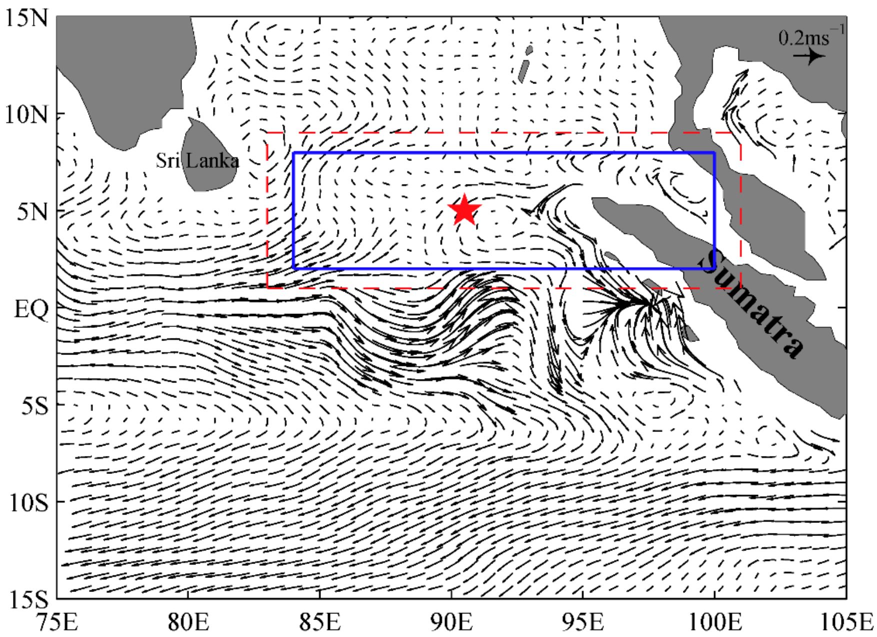

Figure 1. The annual climatology of surface currents (vector; m s^{-1}) from OSCAR during 2001-2014. The red star denotes the mooring location. The blue solid rectangle marks the region of 2°N-8°N, 84°E-100°E, where wind stress forcing is 105-day low-pass filtered in the NoLOCAL experiment (Section 2). The area between blue solid rectangle and red dashed rectangle is the transient zone, where the daily wind stress outside the box gradually transits to the 105-day low-pass filtered forcing inside the box.

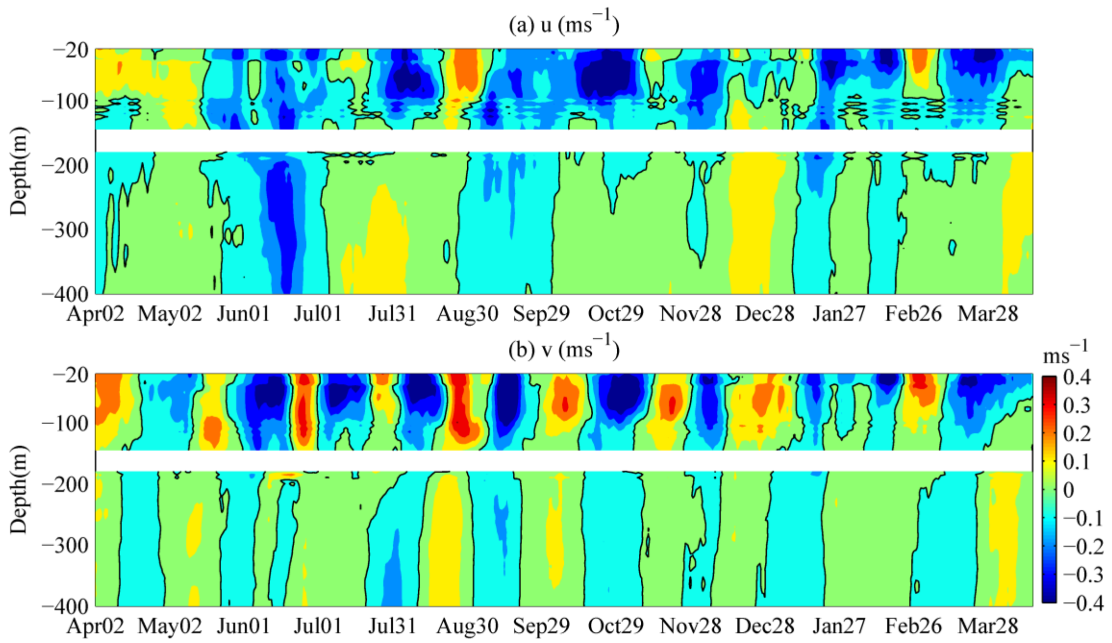

Figure 2. Mooring-observed daily (a) zonal current *u* and (b) meridional current *v* (m s^{-1}) of the upper 400 m at 5ºN, 90.5ºE from April 2, 2013 through April 15, 2014. The black line marks 0 velocity contour.

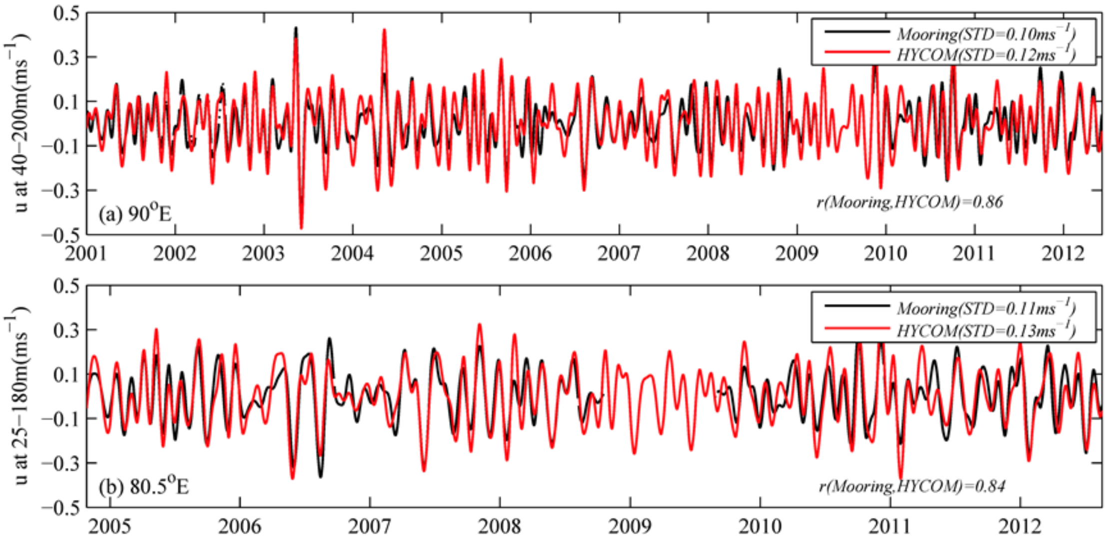

Figure 3. (a) Time series of 40-200 m averaged intraseasonal zonal currents (30-105 day band-pass filtered) at 0, 90°E from RAMA (black line) and HYCOM (red line). (b) Same as (a) but for 25-180 m at 0, 80.5°E.

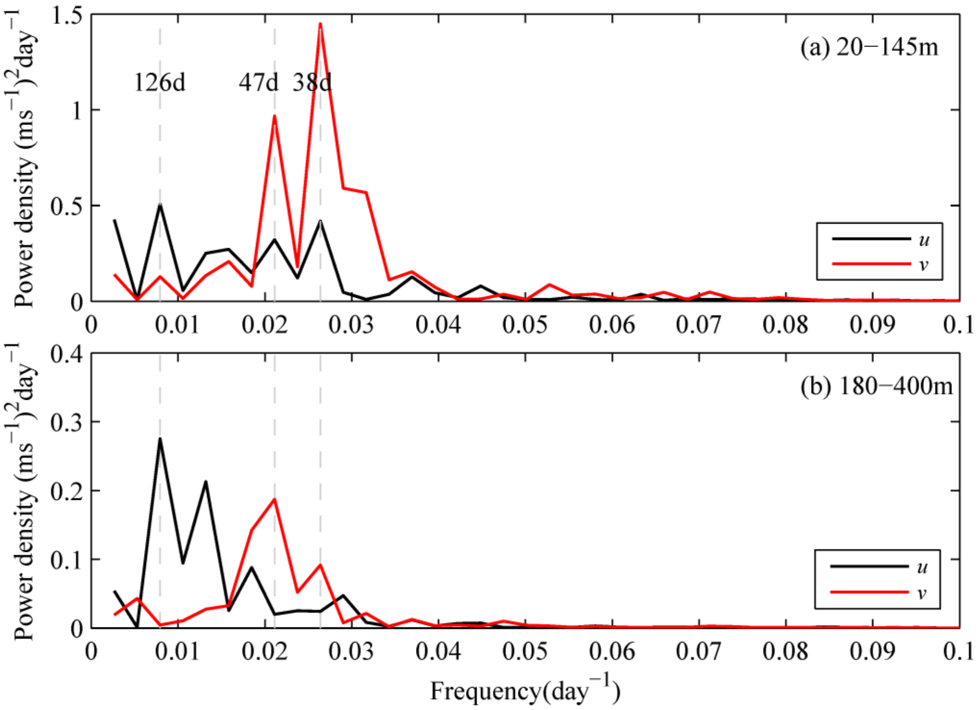

Figure 4. The power spectrum of *u* (black) and *v* (red) averaged over (a) 20-145 m and (b) 180-400 m observed by the mooring at 5 ºN, 90.5ºE.

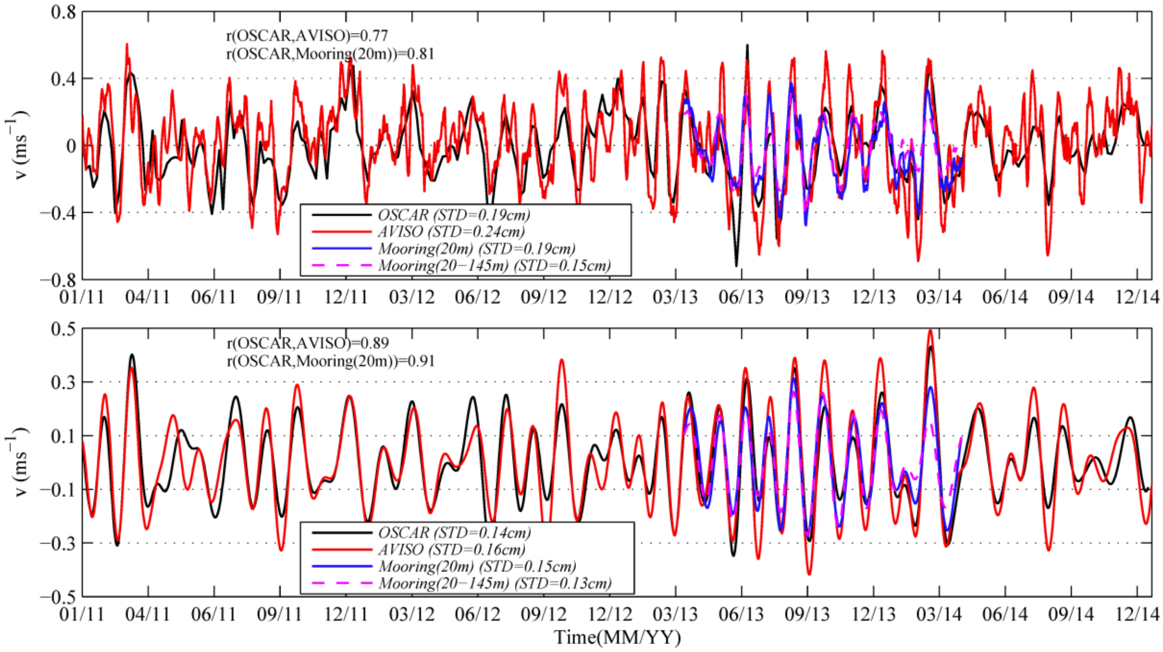

Figure 5. (a) Daily time series of the surface *v* from OSCAR product (black) and surface geostrophic meridional current from AVISO (red) during January 2011-December 2014, and 20 m (blue) and 20-145 m averaged (dashed-pink) *v* from the mooring measurements during April 2013- April 2014, at 5ºN, 90.5ºE. (b) Same as (a) but for the 30-105 day band-pass filtered currents.

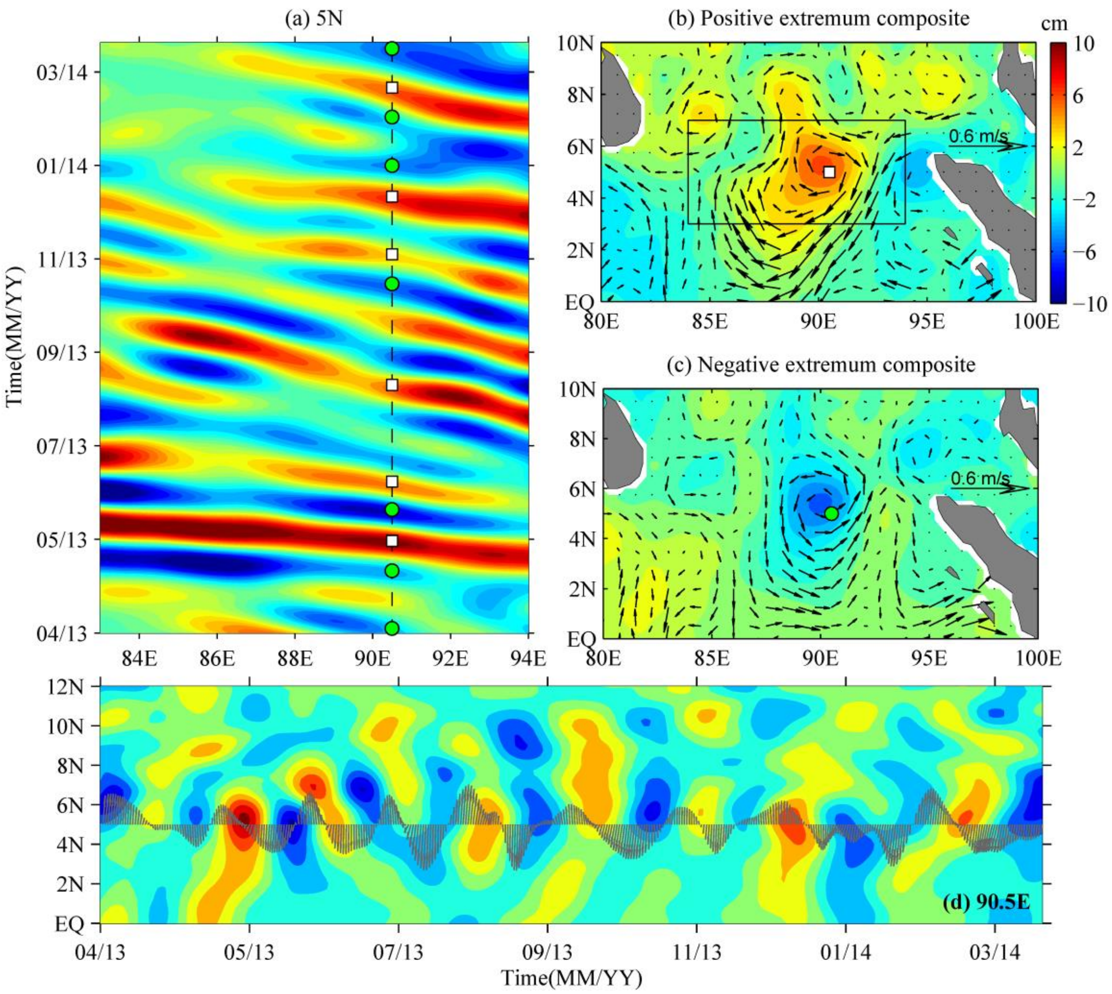

Figure 6. (a) Time-longitude plot of intraseasonal SSHA along 5°N during April 2013-April 2014. White squares and green circles denote peaks of positive and negative SSHA events at the mooring site (5°N, 90.5°E) exceeding one STD magnitude. (b) Intraseasonal SSHA and currents for the composite of the positive SSHA events. The black box shows the region covers the 3°N-7°N, 84°E-94°E. (c) Same as (b) but for the negative SSHA events. (d) Time-latitude plot of intraseasonal SSHA at 90.5°E. Superimposed on the SSHA are velocity vectors observed by the mooring at 5°N, 90.5°E from a depth of 20 m.

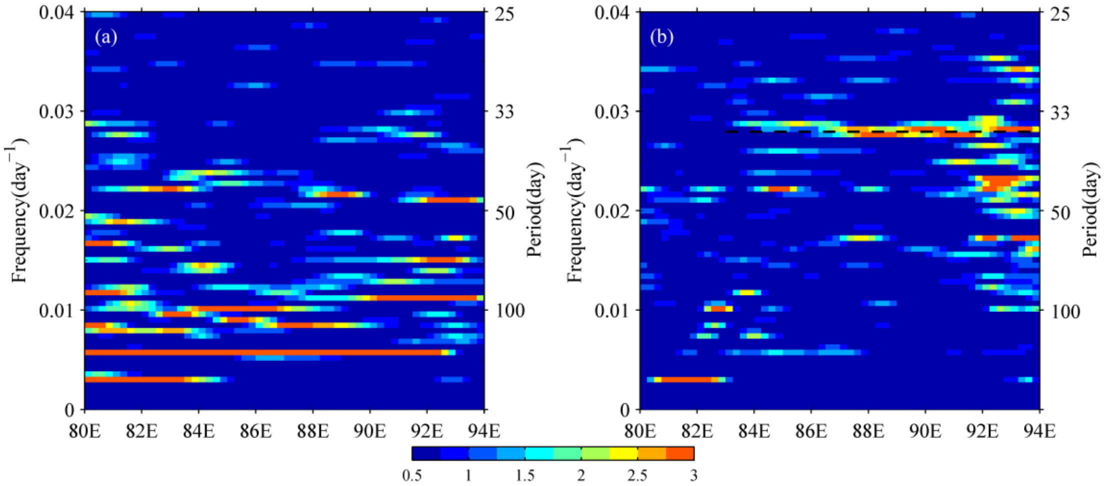

Figure 7. Power spectra of (a) *u* and (b) *v* along 5°N based on daily AVISO surface geostrophic current. The black dashed line in (b) denotes the peak at 36 day period.

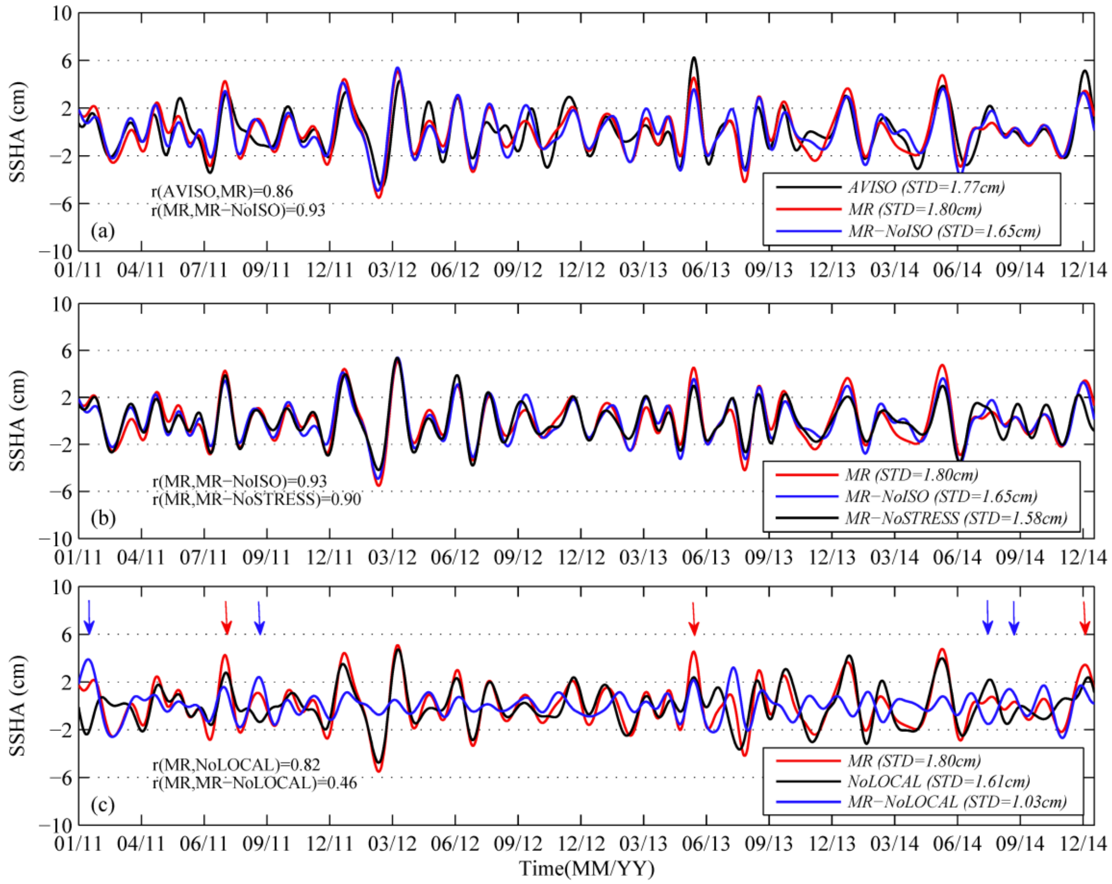

Figure 8. (a) Time series of intraseasonal (30-105 day band-pass filtered) SSHA averaged in the 3°N-7°N, 84°E-94°E (black box in Fig. 6b) from the AVISO, HYCOM MR and the solution difference, *MR-NoISO* (measuring the total ISO forcing effect) for 2011-2014. (b) Same as (a) but from the MR, *MR-NoISO*, and *MR-NoSTRESS* (measuring wind stress effect). (c) Same as (a) but from MR, NoLOCAL (measuring remote forcing effect), and *MR-NoLOCAL* (blue line; measuring local forcing effect).

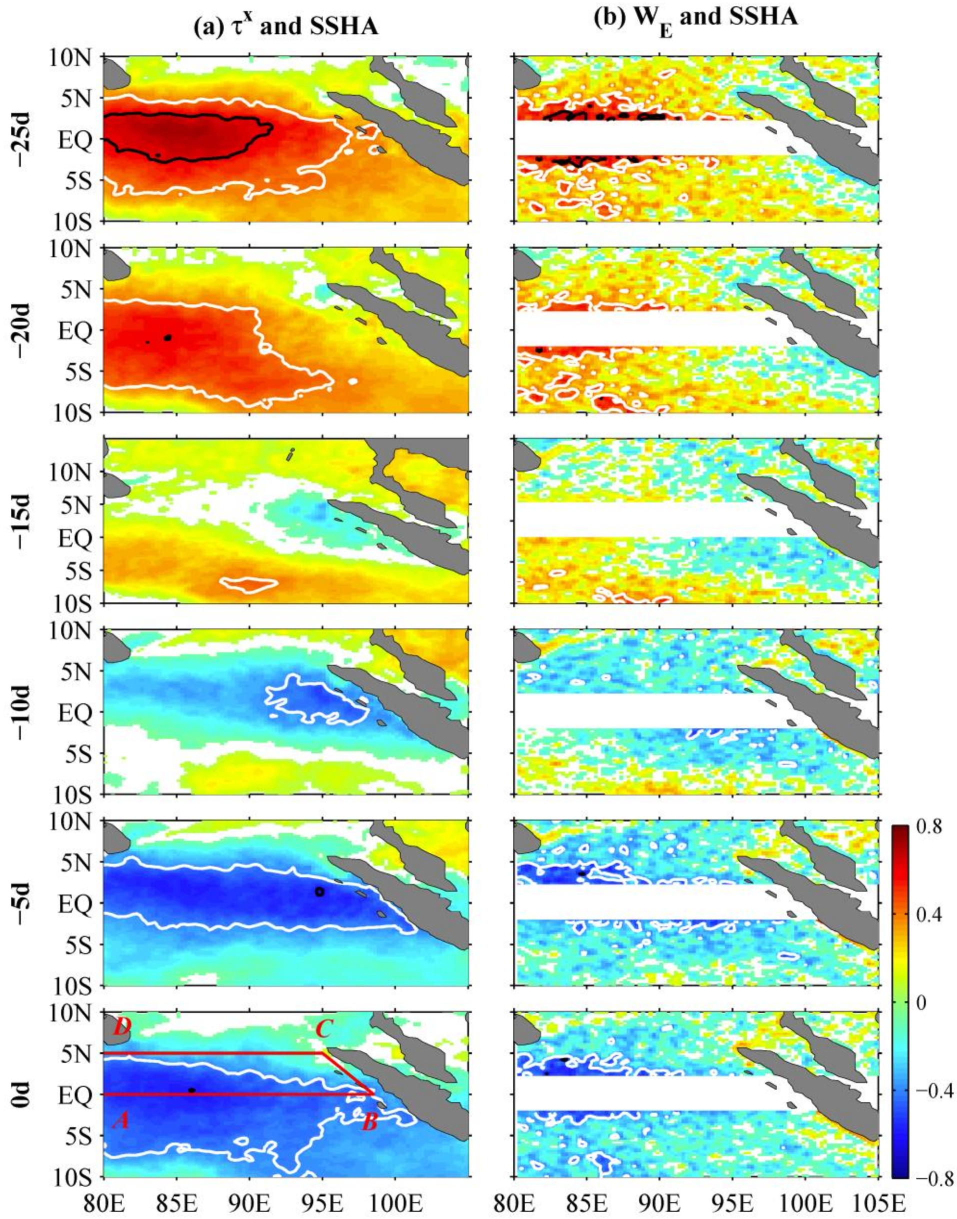

Figure 9. (a) Correlation coefficients between intraseasonal ASCAT zonal wind stress τ^x at each grid point and intraseasonal AVISO SSHA averaged over 3°N-7°N, 84°E-94°E (black box in Fig. 6b) when τ^x leads SSHA by 25, 20, 15, 10, 5, and 0 days. The black (white) contours represent 0.6 (±0.4) correlations. Correlation values below 95% significance level are masked white. (b) Same as (a) but for the correlations between intraseasonal Ekman pumping velocity W_E and box-averaged SSHA. The red lines in (a) denote routes along the equator (from A to B), along the coasts of Sumatra

(B-C), and along 5°N (C-D). Longitudes of A-D are 80°E, 98.5°E, 95°E, and 80°E, respectively.

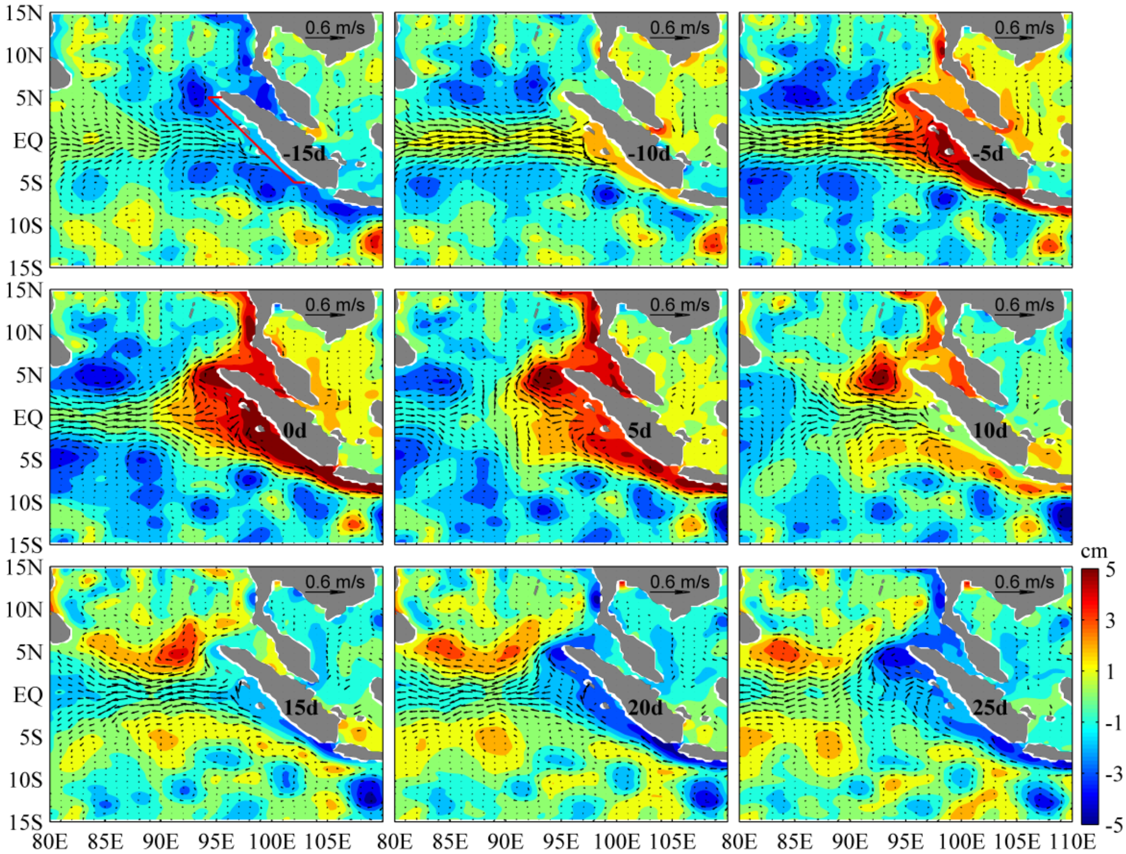

Figure 10. Composite intraseasonal AVISO SSHA (color; cm) and intraseasonal OSCAR currents (vectors; m s^{-1}) of the positive SSHA events during 2011-2014, with a 5-day interval. The 0 day is defined by the SSHA maximum along the Sumatra coast (within one-longitude of the Sumatra coast between 0°-5°N, shown in the -15 day map). The high SSHA events are identified with a criterion of SSHA exceeding the STD value.

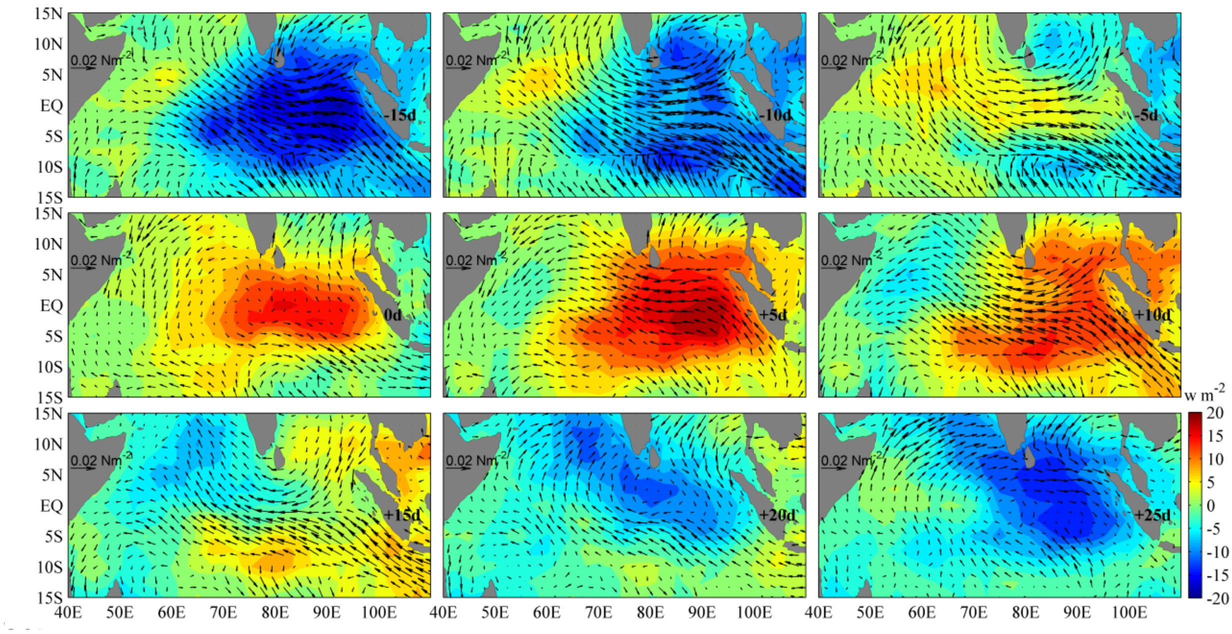

Figure 11. Composite intraseasonal (30-105 day filtered) OLR anomaly (color) and intraseasonal wind stress anomaly (vectors) in the tropical Indian Ocean corresponding to the positive SSHA events during 2011-2014.

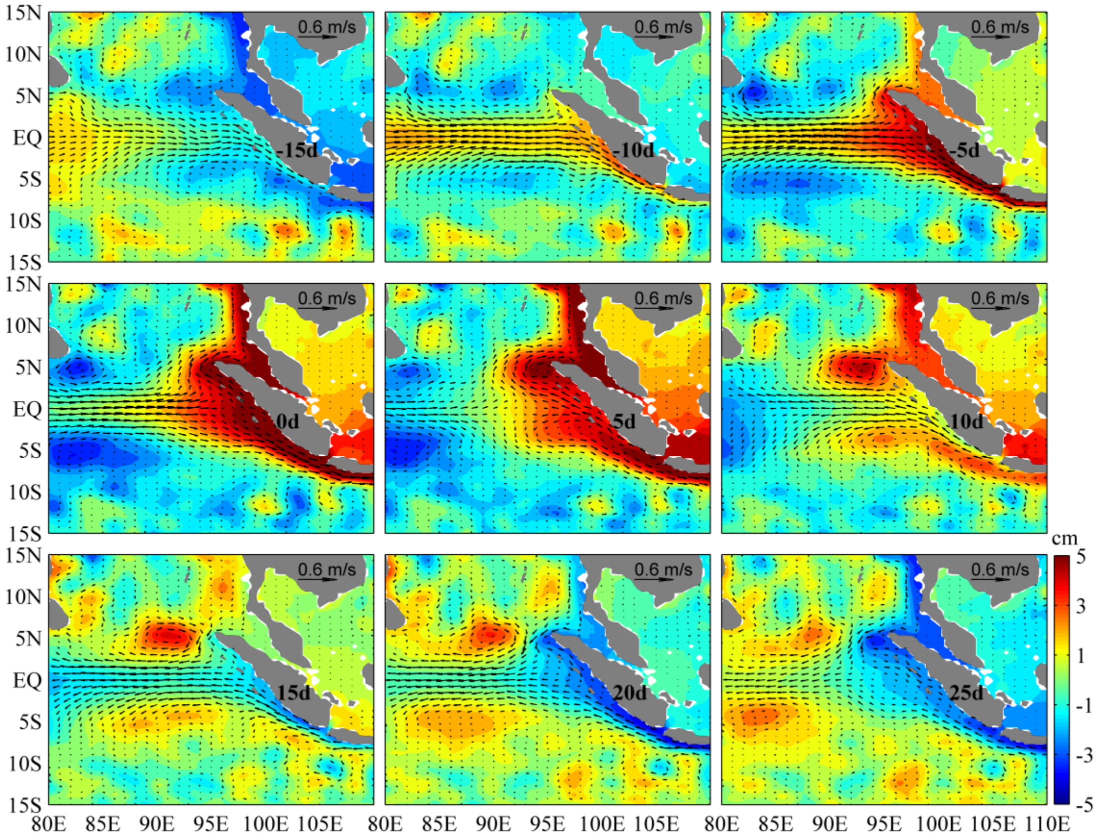

Figure 12. Same as Figure 10 but based on NoLOCAL experiment.

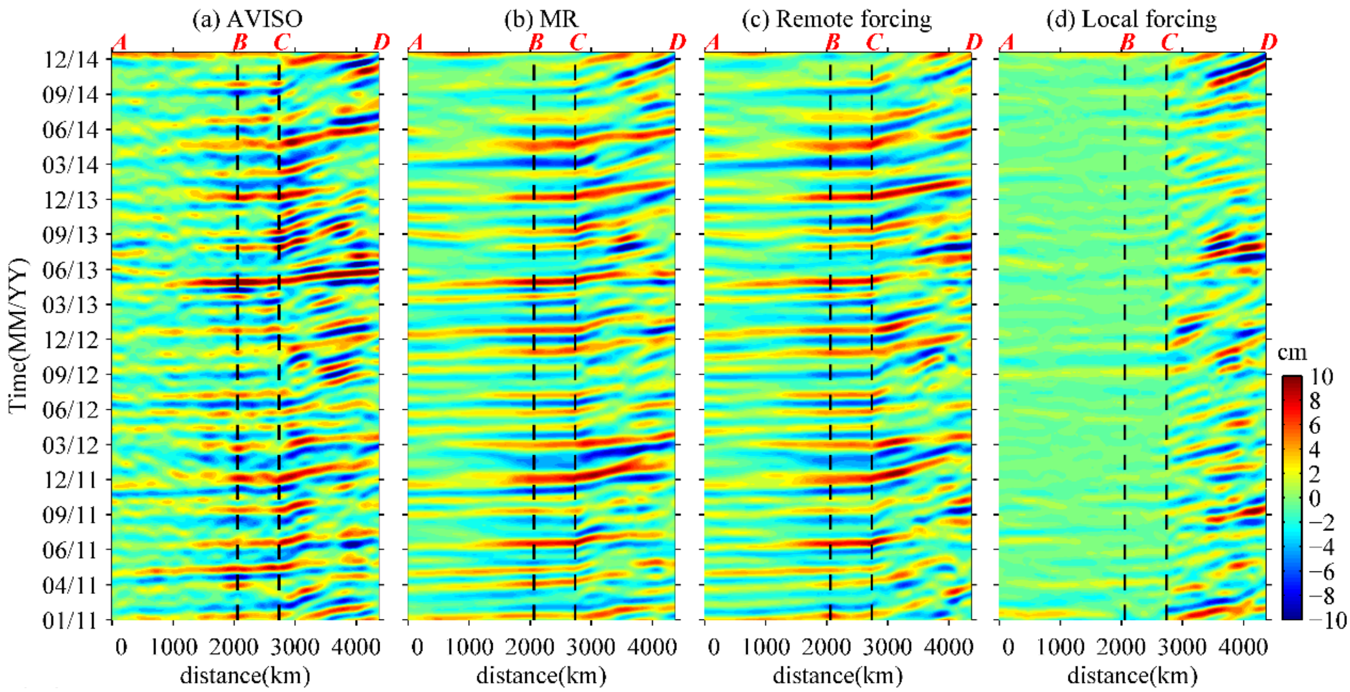

Figure 13. (a) Time-longitude plots of intraseasonal (30-105 day band-pass filtered) SSHA from AVISO along the red lines shown in Figure 9a. (b)-(d) are the same as (a) but for SSHA from (b) the MR, (c) the NoLOCAL experiment measuring the remote wind forcing effect, and (d) their difference *MR- NoLOCAL* that assesses the local forcing effect.

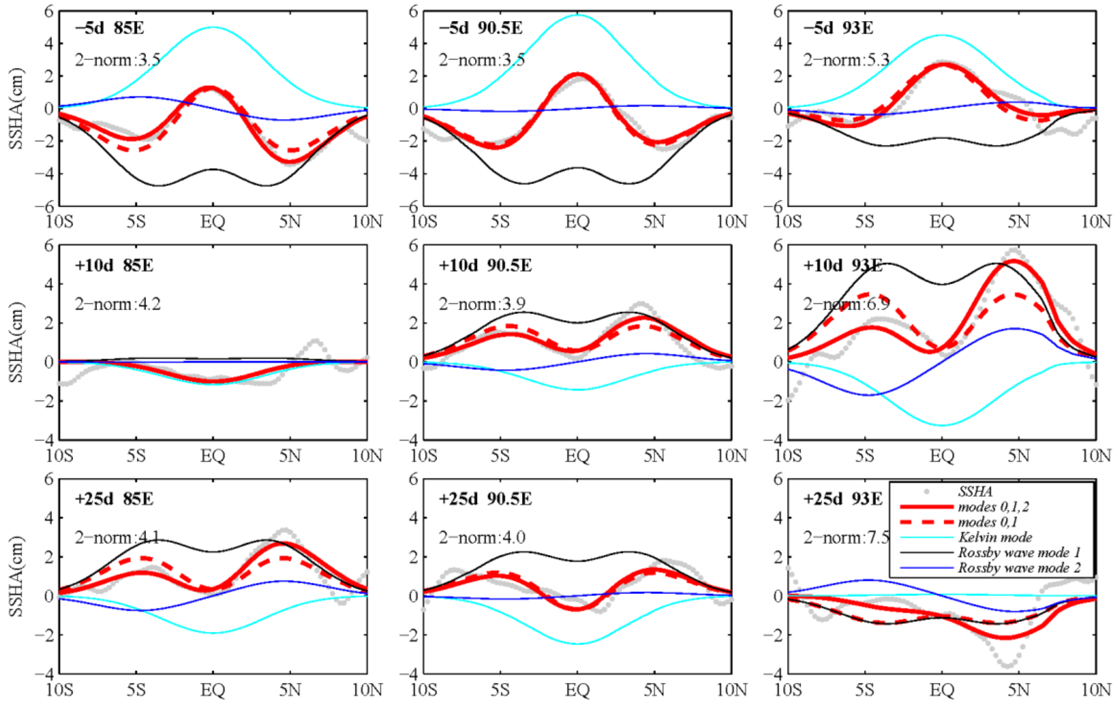

Figure 14. Meridional distributions of intraseasonal SSHA along 85°E, 90.5°E and 93°E on -5 day, +10 day and +25 day. Grey dots are the composite SSHAs shown in Figure 10. Red solid, red dashed, cyan, black, and blue curves are superposition of the first three meridional modes, superposition of the first two meridional modes, the Kelvin wave meridional mode, the first meridional symmetric Rossby wave mode, and the second meridional anti-symmetric Rossby wave mode, respectively.

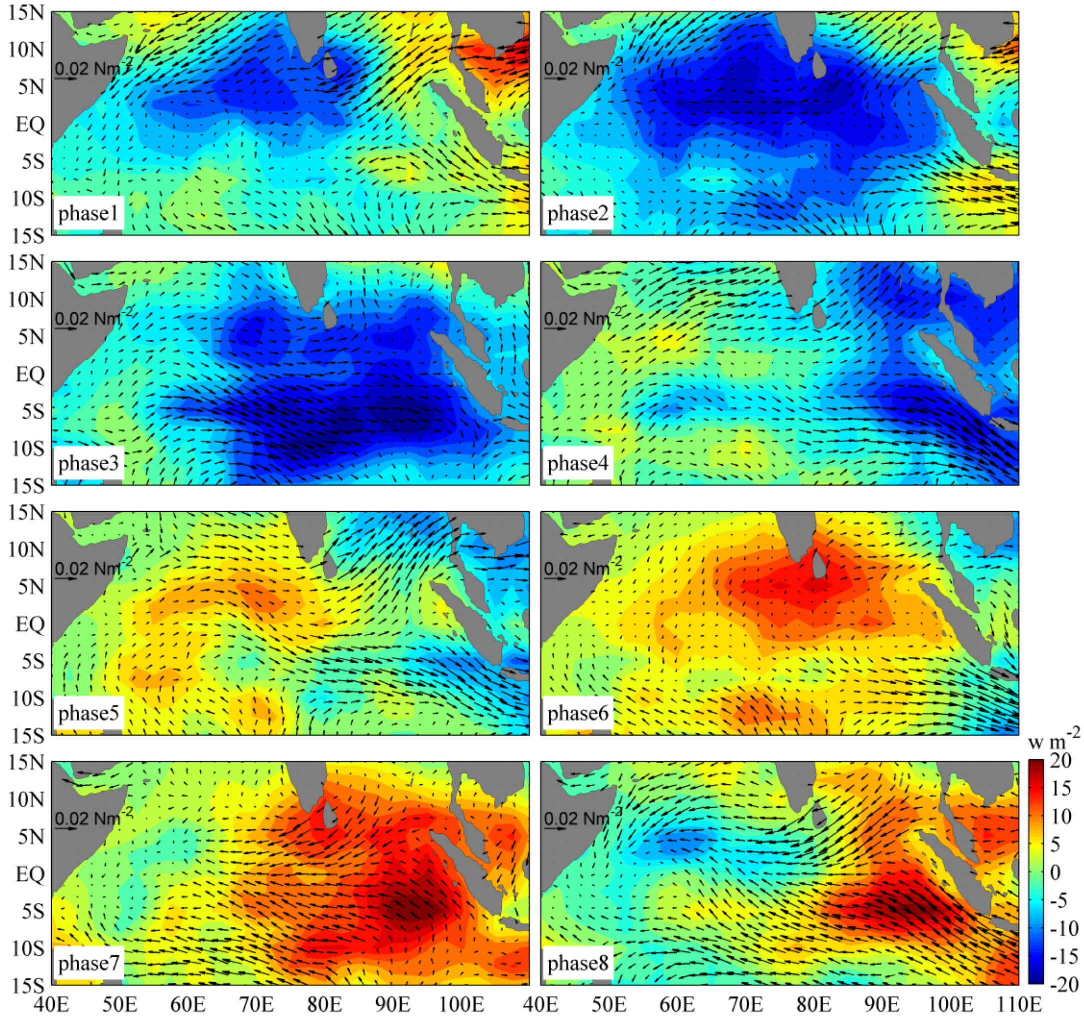

Figure 15. Composite intraseasonal wind stress anomaly (vectors) and OLR anomaly (color) for eight phases of the RMM index.

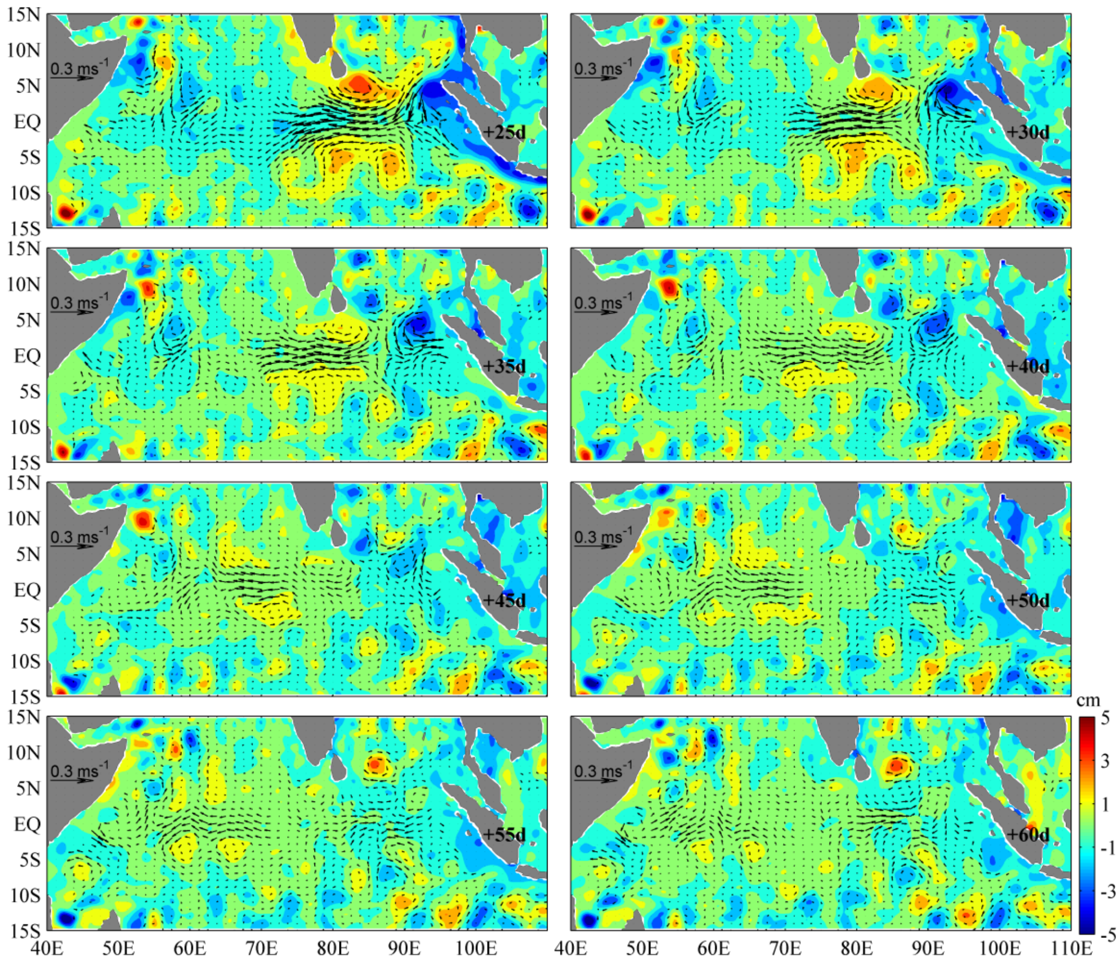

Figure 16. Same as Figure 10 but for the tropical Indian Ocean from +25 day to +60 day.

Figure 1

Click here to access/download
Non-Rendered Figure
Figure 1.pdf

Figure 2

Click here to access/download
Non-Rendered Figure
Figure 2.pdf

Figure 3

Click here to access/download
Non-Rendered Figure
Figure 3.pdf

Figure 4

Click here to access/download
Non-Rendered Figure
Figure 4.pdf

Figure 5

Click here to access/download
Non-Rendered Figure
Figure 5.pdf

Figure 6

Click here to access/download
Non-Rendered Figure
Figure 6.pdf

Figure 7

Click here to access/download

Non-Rendered Figure

Figure 7.pdf

Figure 8

Figure 9

Click here to access/download
Non-Rendered Figure
Figure 9.pdf

Figure 10

Click here to access/download
Non-Rendered Figure
Figure 10.pdf

Figure 11

Click here to access/download
Non-Rendered Figure
Figure 11.pdf

Figure 12

Figure 13

Click here to access/download
Non-Rendered Figure
Figure 13.pdf

Figure 14

Click here to access/download
Non-Rendered Figure
Figure 14.pdf

Figure 15

Figure 16

Click here to access/download
Non-Rendered Figure
Figure 16.pdf